Master of Science Thesis

Study of Skin-Stringer Separation in Postbuckled Composite Aeronautical Panels

L.J. Kootte

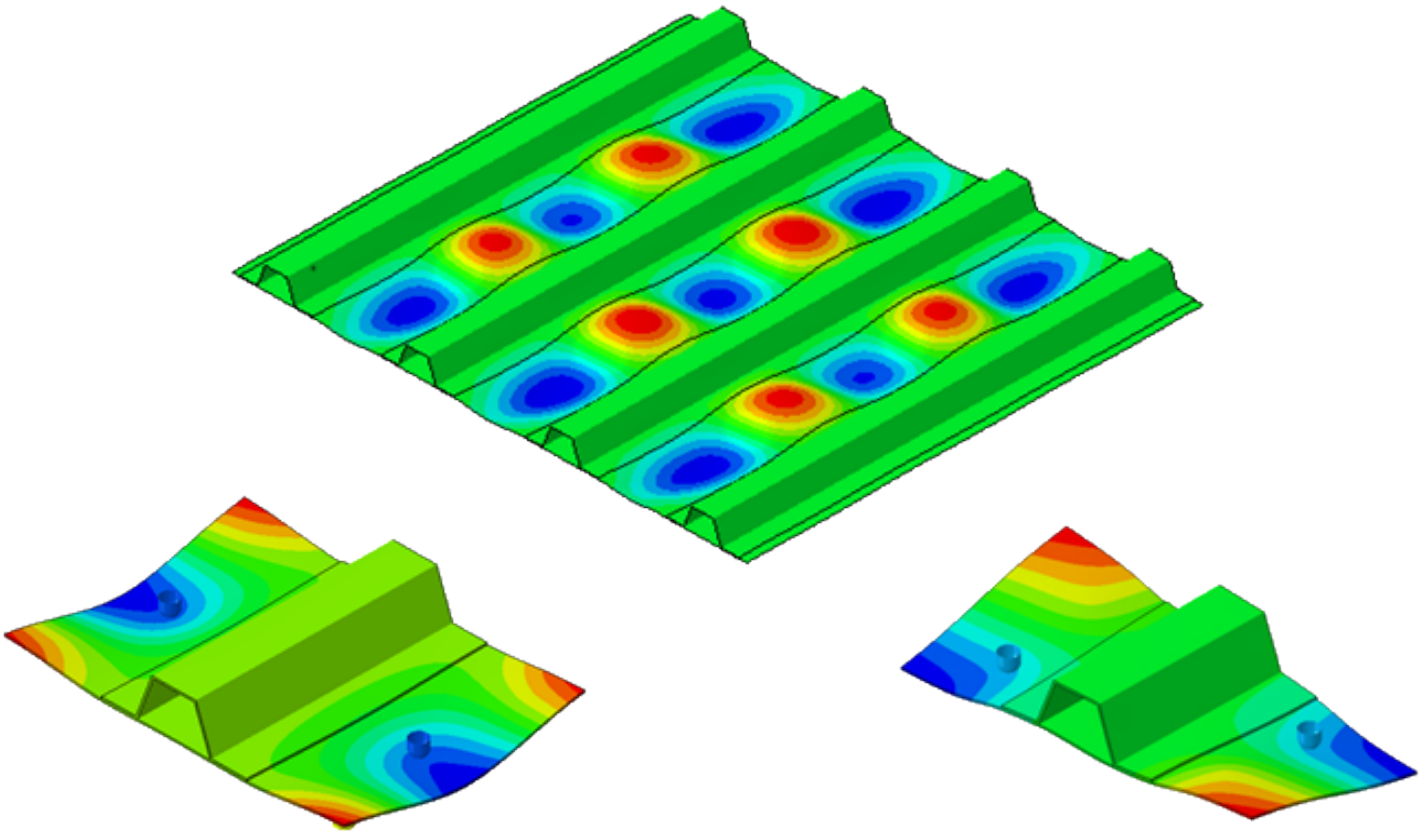

Faculty of Aerospace Engineering · Delft University of Technology

TU Delft Delft University of Technology

Study of Skin-Stringer Separation in Postbuckled Composite Aeronautical Panels

Master of Science Thesis

For obtaining the degree of Master of Science in Aerospace Engineering
at Delft University of Technology

L.J. Kootte

11^{th} July 2018

Faculty of Aerospace Engineering · Delft University of Technology

Delft University of Technology
Faculty of Aerospace Engineering
Department of Aerospace Structures and Materials

GRADUATION COMMITTEE

Dated: 11^{th} July 2018

Chair holder:

Prof. Dr. Chiara Bisagni

Committee members:

Dr. Sergio R. Turteltaub

Dr. Dimitrios Zarouchas

Dr. Carlos G. Dávila

Abstract

Aeronautical composite stiffened structures have the capability to carry loads deep into post-buckling, yet they are typically designed to operate below the buckling load to avoid potential issues with durability and structural integrity. Large out-of-plane postbuckling deformation of the skin can result in the opening of the skin-stringer interfaces, especially in the presence of defects, such as impact damage. To ensure that skin-stringer separation does not propagate in an unstable mode that can cause a complete collapse of the structure, a deeper understanding of the interaction between the postbuckling deformation and the development of damage is required. The present study represents a first step towards a methodology to assess and improve the capabilities of stiffened composite structures subjected to postbuckling deformations.

Two regions are identified in a four-stringer panel in which skin-stringer separation can occur, namely the region of maximum deformation and the region of maximum twisting. Both regions are studied using a finite element model of a representative single-stringer specimen. For the region of maximum deformation, a seven-point bending configuration is used, in which five supports and two loading points induce buckling waves to the specimen. The region of maximum twisting is approximated using an edge crack torsion configuration, with two supports and two loading points. These two configurations are studied by changing the positions of the supports and the loading points. An optimization procedure is carried out to minimize the error between the out-of-plane deformation of the representative single-stringer specimen and the corresponding region of the four-stringer panel.

The optimal configurations are applied to a finite element model of a single-stringer specimen including cohesive elements to simulate damage initiation. The types of damage initiation that occur in these configurations are compared to the global/local analysis of the two identified regions of the four-stringer panel. Furthermore, the effect of the position of the supports and loading points on damage initiation is investigated. The edge crack torsion configuration that is found to be the best at approximating the twisting deformation of the panel also shows the most similarity in damage characteristics with respect to the four-stringer panel.

Table of Contents

List of Figures

List of Tables

List of Acronyms

3PB	Three point bending
4PB	Four point bending
6PBP	Six point bending plate
7PB	Seven point bending
ASTM	American Standard for Testing Methods
B-K	Benzeggagh-Kenane
CFRP	Carbon fiber reinforced plastic
COH3D8	Eight-noded cohesive element
CZM	Cohesive zone model
ECT	Edge crack torsion
ENF	End-notched flexure
FE	Finite Element
PRSEUS	Pultruded Rod Stitched Efficient Unitized Structure
RSS	Residual sum of squares
S4R	Four-noded conventional shell element with reduced integration
SC8R	Eight-noded continuum shell element with reduced integration
SSC	Single stringer compression
VCCT	Virtual crack closure technique

Preface

With my prior experience as a structural engineer at the Delft Human Power Team, I started my Master in Aerospace Structures and Materials. During the course on buckling of structures, which was taught by my supervisor Prof. Bisagni, I knew what I wanted to do for my thesis research. The topic on strength after buckling, especially for composite structures, has so much potential for the future of aeronautics. Prof. Chiara Bisagni proposed a topic on modeling skin-stringer separation in postbuckled structures, which I gladly took.

During the first week of my literature study, I had the chance to talk to a senior researcher on this specific topic, Dr. Carlos Dávila. He shared his knowledge with me and showed me the gaps in the currently available literature. This is when the interest in the effect of skin twisting on skin-stringer separation arose.

Prior to my thesis, I did an internship at ATG Europe, where I was responsible for developing Python tools that helped with the pre- and post-processing of finite element results. This experience helped me to develop similar tools for this research. I have tried to limit the repetitive work by creating Python tools. This helped me to achieve and learn more in the end.

This is what led to this final document, which is my Master thesis. I hope that you will enjoy reading it as much as I did researching it.

Acknowledgements

I would like to thank...

- my supervisor Prof. Chiara Bisagni for her time, patience and assistance during my thesis. She has been a great source of information, which helped to improve my research. She always knew how to help me to go the extra mile, either convincing me wrong when I was stubborn or giving me a motivational speech.
- Dr. Vipul Ranatunga, Dr. Carlos Dávila and their colleagues who provided us with the tools to start this research and with their experiences and guidance.
- Laura for all her help and support, your presence brings joy to the department.
- my friends and colleagues from my master: Eva, Guyonne, Steven, Bram, Katleen and Lander and my friends from the bachelor: Tom, Tijmen, Joost and Aalok. They have supported me during the long period of starting my bachelor to finishing my thesis. The numerous coffee breaks during the day and drinks in the evening helped me to express my frustration and keep me sane. You made university fun.
- my highschool friends and roommates. They made coming home after a long day of work always very enjoyable. There was always someone home to relax and listen to all my complaints.
- my parents for supporting me both financially and emotionally. They have always handed me the right tools and advice to strive for the best.
- my best friend Marc, because of him I have started the journey of becoming an aerospace engineer and because of him I am able to finish it.
- Special thanks goes to my friend and colleague Kevin van Dooren. The nine months that we have spend together in the office working on our theses resulted in lots of interesting discussions. We have shared our knowledge on Abaqus and advised each other during dilemmas. I hope this will continue in our coming years as PhD candidates.
- Last, but certainly not least, I want to thank my girlfriend Linda, who has been by my side during the highs and the lows. There is no one that has read my literature study, thesis and first paper as often as she has.

Delft, University of Technology — L.J. Kootte
11^{th} July 2018

"Nowadays everyone wants to have an impact,
except the people that work with composites."

— *Luc Kootte*

Chapter 1

Introduction

Aeronautical composite stiffened structures are typically designed to operate at loads below the buckling load to ensure durability and structural integrity. The interaction of complex failure modes, which is inherent to composites, in combination with the large out-of-plane displacement of the skin associated with buckling, can result in skin-stringer separation. To design aeronautical structures that can operate in postbuckling without the possibility of unstable skin-stringer separation, a deeper understanding of the interactions between structural and material response is necessary.

A number of studies can be found in literature on simplified specimens that are representative of critical loading conditions. The three point bending (3PB) test, in which out-of-plane deformation is applied to a specimen with a skin and a co-bonded or co-cured doubler, is representative of the opening mode of a stringer flange that results from a combination of the high deformation of the skin and the mismatch in flexural stiffness of the skin and stringer. A similar type of damage is also investigated using a seven point bending (7PB) test, which adds the complex interaction of the buckling deformation of the skin. The 7PB test consists of a single-stringer specimen, where five supports and two loading points apply out-of-plane deformation to the skin. The resulting deformation is similar to a half-wave-long section of a postbuckled multi-stringer panel. A third test that does account for in-plane compressive stresses is the single-stringer compression test, which represents the stress state of a full-size panel. These tests will be discussed in more detail in Chapter 2.

In all these tests, it is expected that the debonding in dominantly mode I of the skin-stringer initiates at the location where the deformation due to the buckling wave is at its maximum. However, in research on skin-stringer separation, a possible skin-stringer separation in mode II + III is also observed due to the twisting of the skin at the inflection point, located in between two buckling half-waves. Inflection points can be critical locations, for example, in structures with a tapered stringer flange termination, where a relatively low flexural stiffness reduces the likelihood of separation in mode I.

The objective of the present work is to develop a methodology that allows the design of a loading configuration that can be applied to a single-stringer specimen to evaluate the different

buckling shapes of composite multi-stringer panels that can lead to skin-stringer separation. The first goal of this effort is to develop specimens that are less expensive to manufacture and test than the corresponding multi-stringer panel. In addition, these specimens should require numerical models that are computationally less demanding than larger structures, which allows the use of finer meshes to investigate the performance of detailed damage models that can predict skin-stringer separation.

In this work, the postbuckling deformation of a four-stringer panel is investigated and two critical regions of the panel are identified, discussed in Chapter 3. Then, specimens representative of these critical locations are designed. The first specimen is representative of the region of the four-stringer panel with maximum out-of-plane deformation. This deformation mode promotes opening of the skin-stringer interface, and it is studied using a single-stringer specimen in a 7PB configuration. The second region is studied using a representative single-stringer specimen in an edge crack torsion (ECT) configuration, where two supports and two loading points are used to create a twisting deformation on the specimen. Different loading conditions of these configurations are defined by altering the positions of the supports and loading points. The out-of-plane deformation of the specimen for each condition is compared to the buckling shape of the corresponding region of the four-stringer panel, discussed in Chapter 4. The next step is to verify that the initiation and propagation of the skin-stringer separation in the single-stringer specimens in the two configurations outlined is similar in location and out-of-plane deformation as in the four-stringer panel. This is investigated using a cohesive-based damage model of the skin-stringer interface, discussed in Chapter 5.

Chapter 2

Literature Study

This chapter presents a brief introduction on composites and buckling induced delaminations in Section 2.1. Furthermore, the building block approach is explained in Section 2.2 and some of the tests that are part of this approach in Section 2.3. Next, the cohesive damage model that is used to model skin-stringer separation is presented in Section 2.4. Finally, a global/local approach is described in Section 2.5, which can be used to decouple the global buckling behavior from the complex separation mechanisms.

2.1 Composites

A fiber reinforce polymer composite is a material type that is widely used in the aerospace industry. It has many benefits such as fatigue and corrosion resistance, low density and is ideal for topology optimization. Due to their anisotropic properties (having high strength in their primary direction) and low density, composites are a useful material to design for the lightest solution. A type of composite that is common in the aerospace industry is the Carbon Fiber Reinforced Plastic (CFRP). Within the context of this research, only continuous fiber reinforced plastics are considered. The fibers can be found as either unidirectional tape or as a weave. The continuous fibers are bound together in a resin matrix, in the aerospace industry this is often a thermoset polymer. One layer of CFRP is called a lamina or ply. These plies are stacked on top of each other, this is called a laminate. This stacking can be done in any arbitrary direction, but the most common orientations are: $0°$, $\pm 45°$ and $90°$. Laminates are formed to sub-structures and finally to structures, an example of CFRPs in increasing size can be seen in Figure 2.1.

An example of a laminate layup is $[0°/\pm 45°/90°]$s. Such a layup can be read as, outer layer of a ply directed at zero degree with respect to the reference system. ± 45 corresponds to the orientation in the positive and negative $45°$ directions. The $90°$ ply is oriented orthogonal to the zero degree ply. The "s" at the end of the layup represents "symmetric", this means that it can also be read as: $[0°/\pm 45°/90°/90°/\mp 45°/0°]$. Using a simple plate as an example for this layup, the zero degree gives it strength if the plate is loaded in the longitudinal direction,

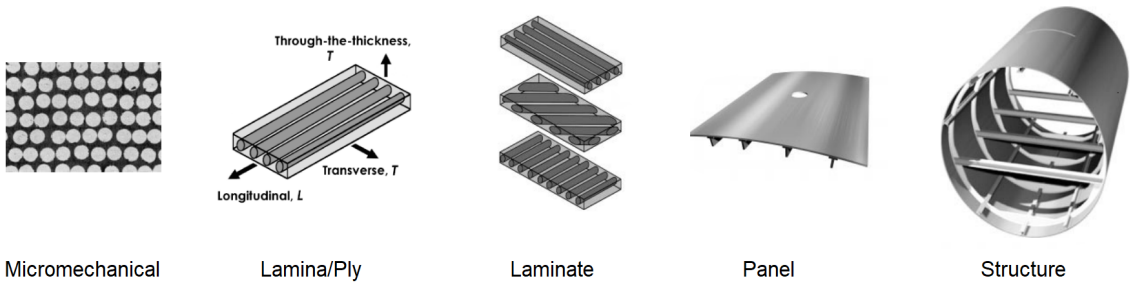

Figure 2.1: Build-up of composites from micromechanical level to full structural level (Taken and edited from [1]).

same holds for the ninety degree plies if loaded in the transverse direction. The ±45° gives the laminate strength for when it is loaded in shear.

Due to the many layers in a laminate, the interfaces of each ply are prone to delamination. During delamination, two lamina open in one or multiple modes that are: mode I (Tensile), mode II (Sliding) and mode III (Scissoring). The different modes can be observed in Figure 2.2. Mode I occurs when high peel stresses are present in a laminate and the plies deform away from each other, creating an actual gap. Mode II is known as sliding shear loading, which occurs due to in-plane shearing. During this failure, two lamina move in the same line but in opposite direction. Finally, mode III occurs when out-of-plane shear is applied to a laminate, it is also known as scissoring or tearing shear. This mode can happen in two ways, either when the two lamina move in the same plane but opposite direction or due to out-of-plane deformation, which can be visualized as tearing a piece of paper. Mode III opening refers to the in-plane scissoring shear within the context of this literature study, unless stated otherwise. The failure modes might exist in an almost pure form during tests, but in structures, mixed mode separations are often observed. The mixed mode I + II has been of interest in many failure modes such as skin-stringer separation during buckling of a structure [2].

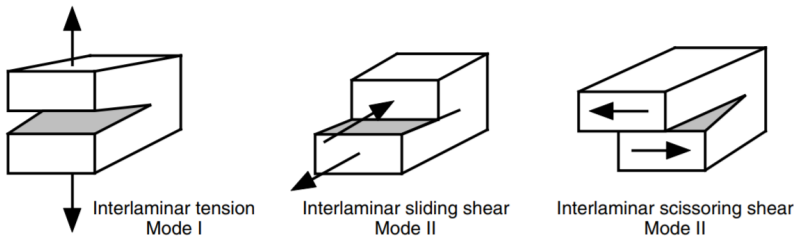

Figure 2.2: Three delamination modes [3].

Before explaining buckling and why skin-stringer separation is such a critical failure mode, the context of these failure modes should be clear. Composite plates are used in the aerospace industry in a more complex configuration; often, a wing or fuselage of an aircraft is made of a thin skin, with co-cured or co-bonded stringers attached to it. The stringers are used to optimize the load carrying capabilities. A stringer is better at resisting out-of-plane deforma-

tion than the skin. This is why they can be applied as panel breakers, where the skin only buckles in between the stringers, increasing the buckling load of a structure.

Buckling can occur during compressive in-plane loading in structures. At a certain load the structure becomes unstable and out-of-plane deformation occurs. A buckling wave pattern depends on many factors such as the intensity of the loading, the boundary conditions and the structure itself. A full buckling wave is similar to a full sinusoidal period, having both positive and negative peaks, as illustrated in Figure 2.3. Often, the term "half buckle wave" is used, which means a half sinus, starting from the midplane of the skin. When using the combination of skin and stiffener, in a good design, the skin buckles before the stiffener does. Upon continued loading, which is called the postbuckling phase, the out-of-plane deformation increases. During this postbuckling phase, the stresses increase at the interface of the stiffener and skin, which can lead to opening consisting of a combination of mode I, mode II and mode III. This phenomenon is still being researched. Allowing postbuckling would decrease the weight of an aircraft, since the structure is still able to carry load after buckling, before such failure starts.

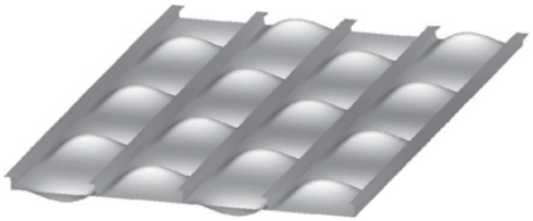

Figure 2.3: Buckling of a stiffened panel [4].

2.2 The Building Block Approach

The building block approach, seen in Figure 2.4 was introduced to meet the need of a standardized testing approach that would reduce the costs and risk of a project [5]. During such a project, testing is required to verify and validate the structural behavior of the product for certification. Testing can be done on multiple (sub-)scales, namely in order of increasing size/complexity: the coupon level, the element level and the panels level. An increase in size and complexity is accompanied by an increase in costs. An optimum has to be found between the costs related to testing and the reliability of its outcome. The properties that are found in a level can be used in subsequent levels as inputs for the analyses or tests. Normally, within the building block approach the lower the complexity/size, the higher the number of tests. If a property of the coupon level is used as an input for the testing of an element, the results of the element test can be incorrect if the property of the coupon level was estimated incorrectly.

Beside the division in levels, there is also the split between experimental tests and numerical analyses. On every level of the pyramid, one could find both experimental and numerical tests. Physical tests can become expensive due to the manufacturing and preparation of the specimens and the occupation of testing equipment. The cost and duration of a project can

be reduced if not only experimental tests are used to verify properties and dependencies such as geometry, loading, environment and failure mode [2]. This section briefly describes the different levels of the pyramid, starting with the coupon level and ending with the full size structure level.

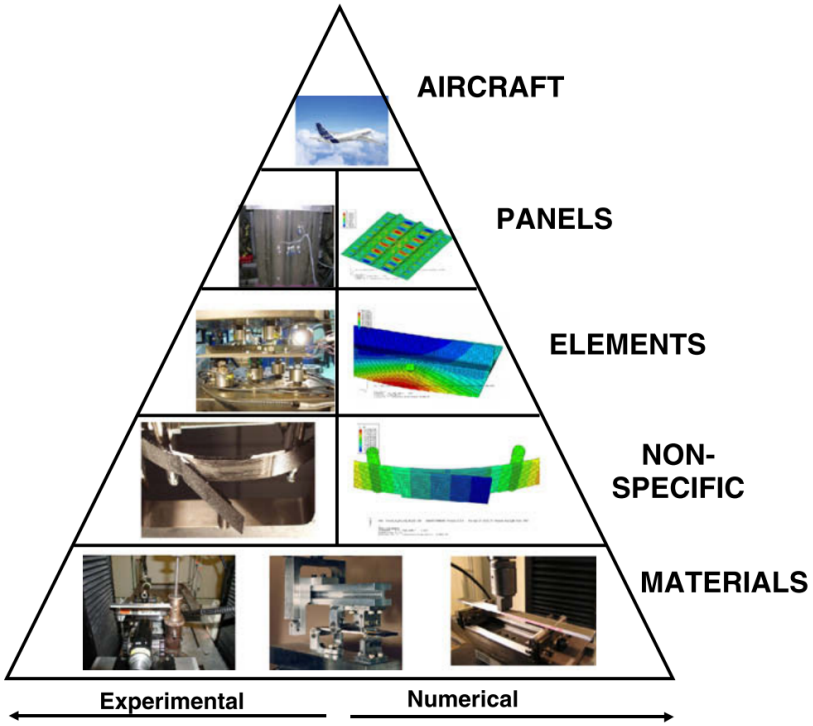

Figure 2.4: Building Block Approach [6].

Coupon level The coupon or materials level, also the lowest block in the pyramid, consists of the smallest and least complex specimens. This level is subdivided into three smaller blocks by the Military Handbook [5]. The first step is to screen and select the materials that are needed for the project. Basic tests are performed on numerous different materials to obtain preliminary values for properties which can be used in a trade-off. In the second step, the material, chosen in the trade-off, is fabricated using different techniques to see how the preliminary properties depend on the process. When a process is settled on, all subsequent tests should conform to the same process in order to not invalidate the specification of the material. The third step is to actually test the material, using the American Standard for Testing Methods (ASTM). The static unnotched material properties and generic notch sensitivity are estimated. Additionally, environmental factor dependencies are researched, such as wet and dry and hot and cold conditions, which are related to the ambient conditions. Preliminary fatigue tests are conducted. Large quantities of these allowable tests are performed to get a statistical dataset for the calculation of material scatter factor and the "A" and "B"-basis allowables.

Element level The element level is the second block, where more complex specimens and test rigs are found. Bertolini et al. [6] have subdivided this level in non-specific specimens

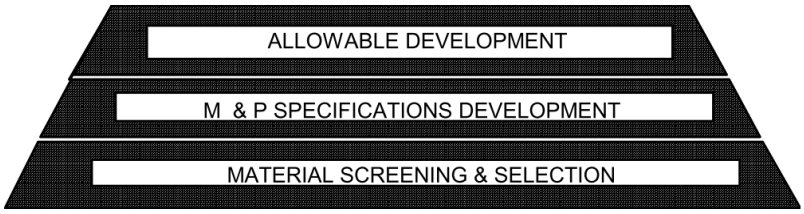

Figure 2.5: Coupon level block used in the military handbook [5]. M&P = material and process.

and element tests. The former serves as a bridge between simple coupon specimens and more complex element specimens. In this level, studies are done on specific technologies, such as the difference in co-cured and co-bonded interfaces. The specimens that are used for testing in this level are often small enough for complex numerical analyses. Using Finite Element (FE) software, a better understanding of the mixed mode delamination of the crack front can be obtained. The size of the specimen is of importance, since a smaller size requires fewer degrees of freedom in a fine mesh. This allows a continuum damage model and cohesive elements to model fiber breaking and delamination. Some analyses can still take up to a few days, if every mechanism is taken into account. Doing experimental tests will show what failure modes need to be taken into account and which could be ignored in the FE model.

The element level is still an unexplored area in the pyramid of the building block approach, specifically for composites. Unlike the coupon level, where many ASTM standard tests are available, the element level lacks standardization on many tests for composite structures. The main objective of the research on this level is to determine the structural properties, which are linked to the properties of the final product. Certain relevant structural properties are the resistance to bearing or the influence of geometry. Complex geometries such as stiffeners and frames are taken into account at this level as well. For example, the crippling load of a stiffener is determined. Crippling occurs when a stiffener is allowed to buckle and the deformation is large enough to break the stiffener. Beside crippling, the stiffener can also debond from the skin. This occurs when the buckling deformation in the skin becomes high enough to initiate skin-stringer separation. Element level tests are reproduced in a FE model to validate the properties and to run test simulations to reduce costs. The properties in the model are obtained in the coupon level tests, such as interface strength and material allowables. Due to the increased size, a full damage model is computationally costly. The experimental tests will show which damage modes should be considered and which should be discarded in the numerical model.

Panels Boundary conditions and loads in this level are representative of what will be seen during the operations of the full structure. When local failure occurs during the testing of a sub-component, the load will be distributed, but it will still keep its load carrying capabilities. The specimens that are used for testing in the aerospace industry consist of multi-stringer skin panels, which can include cut-outs or damage. They may be loaded in tension, compression, bi-axial, shear or any combination of those. The out-of-plane deformation that occurs during this loading is characteristic for the full structure as secondary loads become increasingly visible. Many of the properties from previous levels are used as an input for this level, and the results from this level can be used as an input for the element level. Failure that occurs

in a multi-stringer panel can be isolated and be further analyzed in the element level. Due to the complexity of failure in composites and the large size of a (sub-)structural level, numerical models can become quite large and inefficient to run. An efficient method to combine the global structural behavior with the local failure in a multi-stringer panel is the global/local approach. This approach will be discussed in Section 2.5, but first some of the experimental tests that are performed on the coupon and element level will be presented.

2.3 Experimental Tests

This section provides the reader with the state-of-the-art on element level tests to characterize the mode I + II delamination failure of composites in postbuckling. The first tests that were used are the three and four point bending test. To overcome the problems that occurred in the three and four point bending test, NLR created the larger seven point bending test rig. The previous three tests depend on out-of-plane deformation to create a buckling shape, but the single-stringer compression test depends on in-plane compression. As skin-stringer separation due to a mode III loading is a potential failure mechanism, the edge crack torsion test done on the coupon level of the building block approach is included and a proposed test for mode II + III testing as well. The literature review is concluded with some remarks.

2.3.1 Three and four point bending tests

The specimens for three and four point bending tests consist of a small skin section with a doubler attached, where the doubler represents the flange of a stiffener. The approximate size of these specimens is 120 mm x 20 mm for the skin and 40 mm x 20 mm for the doubler [7,8]. The specimens in Figure 2.6 and Figure 2.7 are flipped for better visualization of the overlap. The three point bending (3PB) test has one central loading line and the four point bending (4PB) test has two off-center, but symmetric loading lines. The outer supporting lines are stationary and the inner loading lines applies vertical displacement on the specimen.

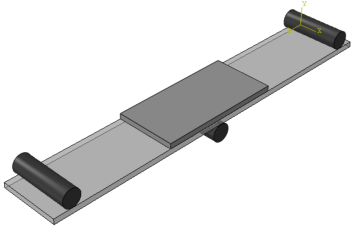

Figure 2.6: Three point bending specimen.

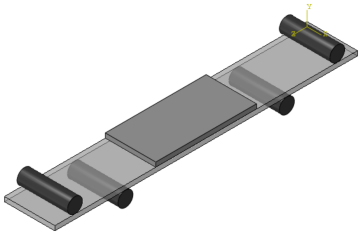

Figure 2.7: Four point bending specimen.

The 3PB is used as a relative simple test set-up that captures the mixed mode I + II opening at the edge of the doubler. For some specimen and set-up configurations, this leads to premature skin failure [8]. Another downside of this test is the catastrophic failure after the initiation of the crack in the 3PB specimens interface [7]. These problems did not occur in the 4PB test

that Minguet and O'Brien [7] used in their same research as comparison. In the 4PB tests a constant moment at the crack interface was present, when the crack itself propagated.

Due to the small size of the set-ups, they are useful for parametric studies. These studies have been done on the following aspects: straight or tapered flange edges, co-cured or co-bonded interfaces and ply orientation at the interface [7]. A tapered edge shows a large resistance to crack initiation, but after initiation, the growth is more abrupt than the straight edges. The co-cured interface often shows a higher resistance to crack initiation than co-bonded interface, but the difference is small compared to the tapered edges. An interface of 0°/0° results in a higher resistance than 45°/-45° [6]. The ply orientation at the interface greatly influences the fracture toughness for onset of delamination, that can be 400% higher than the standard 0°/0°, which is used in the coupon tests [9].

The 3PB and 4PB are used for parametric tests and complex FE modeling. However, the major drawback of both tests is the width dependency of the specimen on the fracture toughness. The crack in the interface nucleates at the free edge and this is not representative of the failure that occurs in a large (multi-) stringer panel [7, 9]. The seven point bending test was developed by NLR [10] in order to solve this problem.

2.3.2 Seven point bending test

The specimen used in the seven point bending test developed by NLR [10] consists of a skin with an attached stringer. The skin is approximately 200 mm x 200 mm in size. The skin is supported from underneath by five supports, one at each corner and one at the center. The specimen is loaded using two loading points that move normal to the skin. The central support and the loading points create a 3PB-like displacement, whilst keeping the rest of the specimen leveled using the other four supports. The out-of-plane deformation mimics the deformation observed in a postbuckled stiffened structure. The shape that is created is equal to one half-wave buckle. The set-up and the created shape can be seen in Figure 2.8(a,b)

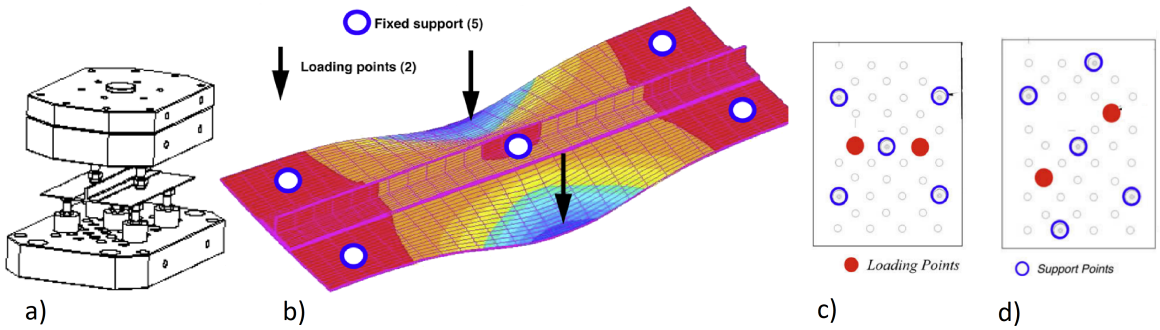

Figure 2.8: Seven point bending test set-up by Bertolini et al. [11]. a) Drawing of the experimental set-up, b) visualization of the out-of-plane displacement, c) configuration for the symmetric set-up, d) configuration for the anti-symmetric set-up.

This 7PB test has received the interest of Bertolini et al. [11], Ye and Chen [12] and Dávila et al. [9]. The main observation in this test was that the crack indeed nucleates at the middle of the specimen, thus away from the free edges as was aimed for by NLR. The second observation

was that the crack initiates at the skin-stringer interface, whereas for the 3PB and 4PB the crack starts often at the first ply above or below the interface [10].

NLR designed this test to reproduce the symmetric buckling shape that results from the compression of a stiffened panel. Bertolini et al. [11] took this a step further and used this both to mimic the symmetrical buckling due to compression, from which the set-up is shown in Figure 2.8c, and skewed buckling due to shear, which is displayed in Figure 2.8d. The experimental results showed a good agreement with respect to the numerical 7PB model.

Bertolini et al. [11] also compared the results from their multi-stringer panel model to the 7PB model. It was shown that the 7PB test is a good method of reproducing the mode I + II delamination, that occurs where out-of-plane displacement is maximum, in a multi-stringer panel. Mode II + III opening, at the inflection point of the buckling wave, was also seen in their multi-stringer panel model. However, mode II + III opening is not tested in the 7PB test and in the previously discussed 3PB and 4PB tests. Mode II + III can be a critical failure mode, if relative flexible stringer flanges are used. The flanges of a hat stringer are often more flexible than of a T-stringer as used by NLR [10], when the test was designed. "Moreover, this presence of mode III brings out the need to develop standardized, reliable characterization methods in order to be able to study the often neglected effects of this mode in greater detail." [11, p. 12].

2.3.3 Single-stringer compression test

The single-stringer compression (SSC) specimen [13] is similar in configuration to the 7PB specimen (Figure 2.9). The specimen size that is used in the research of Bisagni et al. [14] is 240 mm x 150 mm. The specimen is embedded in a resin potting at the top and bottom, which is used to distribute the loading. The bottom is fixed, while the top of the specimen is loaded under in-plane compression. All previously discussed tests apply out-of-plane displacement to load the specimen, whereas the SSC test is based on in-plane compression. The compression of the SSC specimen results eventually into buckling. Multiple buckling half waves are present over the length of the specimen.

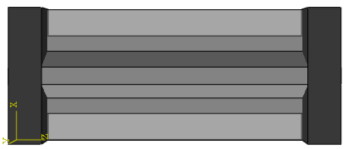

Figure 2.9: Single-stringer compression specimen.

The SSC test is used in the Pultruded Rod Stitched Efficient Unitized Structure (PRSEUS) program [15–17]. They use the test to assess the postbuckling strength of a stringer that is stitched through-the-thickness to the skin. Using side-constraints the edge of the skin is not able to buckle at the free edges. In a multi-stringer panel, those edges are actually constrained by its surrounding materials. With the use of the stitches, delaminations are arrested after initiation. This leads to an efficient structure with a high postbuckling ratio,

prior to failure [18]. However, more research is needed to better understand the concept of postbuckling delamination in order to verify and validate these composite structures.

In a further study of the SSC test [14, 19–22], the choice was made to leave the sides of the specimen unconstrained as opposed to the design of the PRSEUS specimen. The buckling of the specimen resulted into three half waves, initially. The skin between the flanges under the hat stringer also buckled. Due to a jump of the buckling mode in this area, a crack initiated. The growth was unstable and lead directly to final failure. The design proved to be a good choice to assess the postbuckling strength of a panel in the element level stage.

The results of a multi-stringer panel were compared to the SSC specimen [20]. Crack initiation in the panel occurred at the inner side of the hat stringer at the maximum deformation of the buckling wave, which was also seen experimentally. This crack initiation was due to peel stresses at the edge and the opening is a combination of mode I and mode II. This is the same mode as tested in the three, four and seven point bending tests. However, at a slightly higher load on the panel, a crack initiated at the inflection point of the buckling wave, which corresponds to a mode II + III opening. In Figure 2.10, on the left, a part of the panel with the out-of-plane deformation contours is shown. On the right, region three and four, where the mode II + III crack has initiated at the inflection point can be seen. This was also observed by Bertolini et al. [11] and these observations resulted in the research following this literature study. The main focus of this postbuckling skin-stringer separation research has always been on the mode I + II opening. To create an element test that is able to capture this mode II + III opening, an understanding is needed of the coupon tests that are done to characterize mode III and mixed mode II + III delamination.

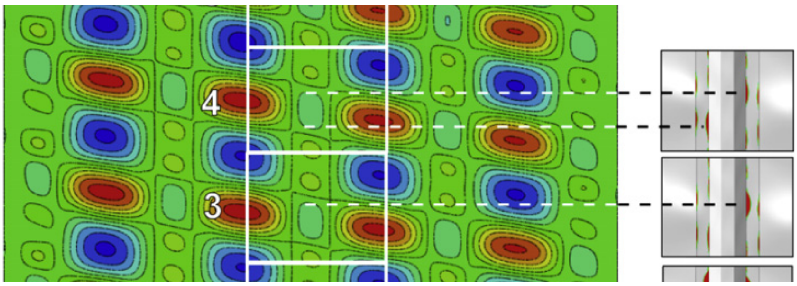

Figure 2.10: Results of the panel showing the debonding at the inflection point [20].

2.3.4 Edge crack torsion test

The split cantilever beam [23–25] and the crack rail shear [26] were among the first tests to be researched for the determination of the mode III critical energy release rate (G_{IIIc}). However, the most promising test is the edge crack torsion test (ECT) [27].

The size of an ECT specimen is approximately 150 mm x 50 mm. Using a Teflon insert during manufacturing, an initial crack is created in the laminate. The commonly used ECT test set-up consists of two supports on the two diagonally across corners and two loading points in the other two corners [28, 29]. When moved down, these loading points create a torsion loading that should lead to a mode III delamination. The specimen with the support and loading points indicated can be seen in Figure 2.11.

To properly assess G_{IIIc}, a pure and constant mode III should be present at the crack interface of the specimen. In all tests the mode I component is negligible. The mode III component is zero at the edges and increases to its maximum at approximately 20% from the edge [30], as seen in Figure 2.12. A mode II component is present near the edges, which can be attributed to the load introduction. The G_{IIc} is lower than G_{IIIc}, with a factor of approximately 2.5. The peak of the mode III component is over 8 times larger than mode II and thus the crack initiation will be purely mode III at the center of the specimen [31]. When minimizing the overhang length, which is the distance between a loading point and the free edge, to approximately 3 mm, the best distribution of mode III was observed. This leads to consistent results over all the tests [32].

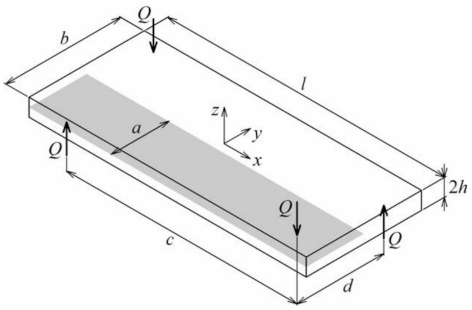

Figure 2.11: Example of a common edge crack torsion test [33].

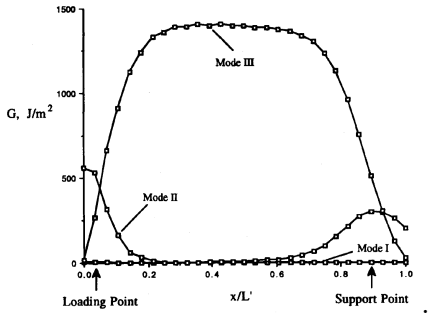

Figure 2.12: Distribution of G_{II} and G_{III} at crack front of the ECT [30].

The unstable crack growth that was observed in the ECT test can be reduced by increasing the ratio of initial delamination per total specimen length (a/b) [31]. Also, increasing the overhang length resulted in a more stable crack growth [32]. The lowest G_{IIIc} occurred at a 0°/45° interface (800 Jm^{-2}) compared to the standard 0°/0° interface with a G_{IIIc} of approximately 940 Jm^{-2} [34], similar to the difference that was seen in 2.3.1.

2.3.5 Six point bending plate test

De Morais and Pereira [35] have investigated a coupon test in mixed mode II + III delamination, which is called the Six Point Bending Plate (6PBP) test. By changing the mixed mode ratio in this test, the results can be extrapolated to a pure mode failure. The pure G_{IIIc} corresponded well with the observations of the mode III tests that were discussed in Section 2.3.4. The most popular test for mode III delamination is the ECT, which loads the specimen in torsion. The mode II critical energy release rate is determined using the End-Notched Flexure (ENF) test [36], wherein the specimen is loaded in bending. A mixed mode II + III would therefore require a combination of both torsion and bending, however this has proven to be difficult. The authors [35] used pure bending to get the mixed mode II + III, with four lower supports of 8 mm diameter and two upper loading points with the same dimensions, shown in Figure 2.13.

Mode II ENF specimens are dominated by 0° UD plies, whereas ECT should have a high number of ±45° plies in order to decrease the change of intraply failure. Two different specimen geometries were used: 150 mm x 40 mm and 100 mm x 60 mm. The former

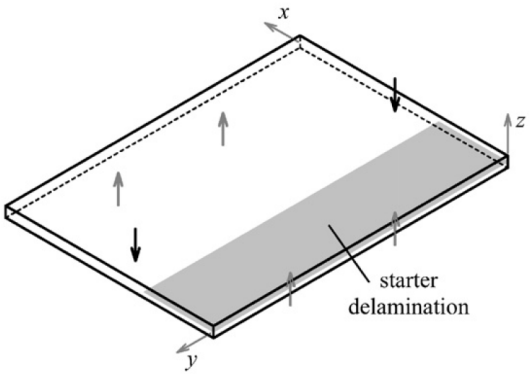

Figure 2.13: Mixed mode II + III six point bending plate test [35].

resulted in a G_{III}/G_T of 0.85 and the latter in G_{III}/G_T of 0.15. G_T is the total energy release rate, $G_I + G_{II} + G_{III}$. The mode I component was near zero along the crack front. The mode distribution of the 0.85 G_{III}/G_T specimen can be seen in Figure 2.14, where y = 0 mm is the edge and y = 75 mm is the middle of the specimen, because the distribution is symmetric before crack initiation. The crack is expected to initiate at the peak away from the edges. The peak (G_{max}) is where G_T is highest. Therefore the average of the curve above 0.9 G_{max} is taken as the fracture toughness when the specimen fails. In Figure 2.15, the mixed mode toughness is plotted against the ratio of G_{III} and G_T. A clear trend is seen that shows an increase in toughness for mode III delamination. When the lines are extrapolated to pure G_{II}, a value of 789 Jm^{-2} is obtained, which is comparable to the ENF test results of 846 Jm^{-2}. More scatter is seen when the G_{III} is increased. The extrapolated G_{IIIc} is between 960 Jm^{-2} and 1070 Jm^{-2}. The conclusion is that $G_{IIc} < G_{IIIc}$ is expected from all the research that has been done in the past.

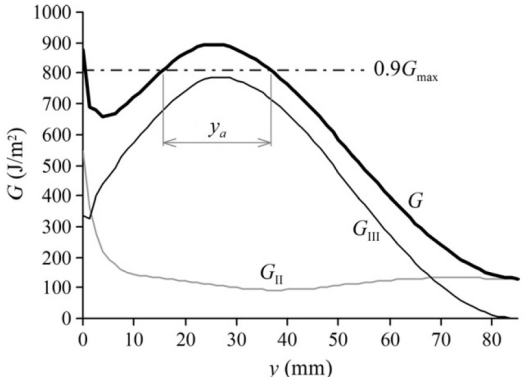

Figure 2.14: Distribution of G_{II} and G_{III} at crack front of the 6PBP [35].

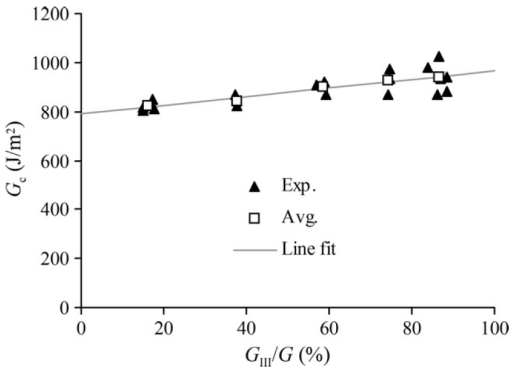

Figure 2.15: Experimental results of the 6PBP with fitting curve [35].

2.3.6 Remarks

For the assessment of mode I + II delamination occurring during postbuckling, the SSC and 7PB are the most promising. The SSC test has the benefit of actually being loaded in

compression to get the desired postbuckling shape. This means that the stress field of the SSC specimen is more likely to be similar to the multi-stringer panel results than the 7PB specimen. The 7PB has a more controlled method of applying out-of-plane deformation and therefore the damage can be followed more closely. More research has been done on the SSC test, but the 7PB is more flexible to changes of the set-up. Bertolini et al. [11] already showed that a different set-up can be used for the testing of shear deformation, which was only done using a picture frame shear set-up so far [18, 37, 38].

2.4 Cohesive Zone Model

Some of these tests described in Section 2.3 were also modeled numerically using FE analyses. In the FE analysis two different damage models were often used, namely the Virtual Crack Closure Technique (VCCT) [39] and the Cohesive Zone Modeling (CZM) [40]. These are used to model the damage at ply interfaces in order to characterize phenomena such as skin-stringer separation. In this research only the CZM will be used, specifically cohesive elements that are characterized the bilinear traction-separation law [41]. These three dimensional cohesive elements can be placed at the interface between the skin and stringer, where the bottom nodes are connected to the skin nodes and the top nodes are connected to the stringer nodes. The relative displacement of the top and bottom nodes results in traction at the interface. A schematic representation of zero-thickness 2D cohesive elements in an undeformed and a deformed state are shown in Figure 2.16. The normal tensile opening is mode I and the sliding shear is mode II, which is shown in Figure 2.2. The single-mode bilinear traction-separation law can be seen in Figure 2.17.

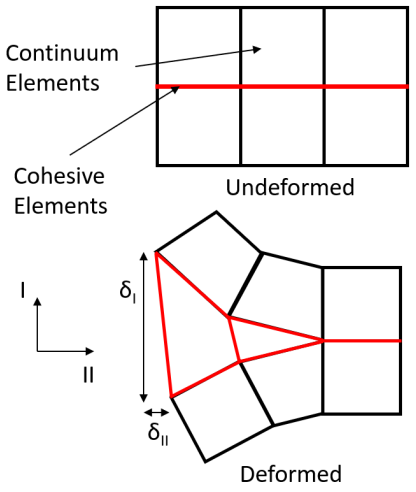

Figure 2.16: Schematic representation of undeformed and deformed 2D cohesive elements.

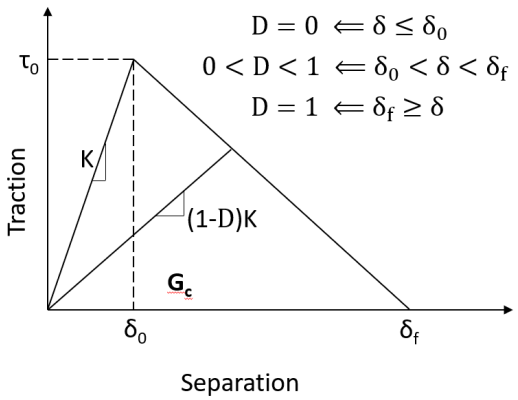

Figure 2.17: Diagram of the single mode bilinear traction separation law

In Figure 2.17, K is the penalty stiffness of the element, τ_0 is the maximum traction that can occur in the element before stiffness degradation starts. The critical energy release rate

(G_c) is the area underneath the curve. δ_0 and δ_f are the relative displacement of the element nodes at which onset of separation starts and when the element is fully damaged. The damage variable D is used for the stiffness degradation of the element, this value is zero before the onset of separation and one when the element is fully damaged. The value of K is often based on previous experiences.

In case of mixed-mode loading conditions, such as mode I + II and mode II + III, which are discussed in Section 2.3, the onset of crack propagation and final failure of the element are dependent on both the normal and shear opening [41]. If the normal traction (τ_I) is compressive, only shear traction (τ_{II} and τ_{III}) is taken into account, because this would lead to crack closing in mode I. This is defined by the MacAuley brackets $< \cdot >$.

$$\left(\frac{< \tau_I >}{\sigma_c}\right)^2 + \left(\frac{\tau_{II}}{\tau_c}\right)^2 + \left(\frac{\tau_{III}}{\tau_c}\right)^2 = 1 \tag{2.1}$$

In the mixed-mode criteria of damage onset, maximum traction for mode I and the shear modes are denoted by σ_c and τ_c, respectively. For the damage initiation, the Benzaggagh-Kenane (B-K) failure criterion [42] is often used for mixed mode conditions:

$$G_{Ic} + (G_{IIc} - G_{Ic}) \left(\frac{G_{II} + G_{III}}{G_T}\right)^{\eta_{BK}} = G_c \tag{2.2}$$

in which $G_T = G_I + G_{II} + G_{III}$ and η_{BK} is the B-K parameter, which is estimated experimentally [43].

The convergence of FE models with cohesive elements is highly dependent on the mesh size of these elements [44]. It is recommended to use at least three cohesive elements in the cohesive zone. The cohesive zone length (l_{cz}) [44] is the distance from the crack front, where the element has reached D = 1, to the element where D = 0. l_{cz} can only be determined during the simulation, but there are some proposed equations that can estimate l_{cz} [45]:

$$l_{cz} = \frac{9\pi}{32} E \frac{G_c}{(\tau_0)^2} \tag{2.3}$$

in which E is the Young's modulus of the material. The size of the cohesive element (l_e) can than be estimated as this is dependent on the number of cohesive elements (N_e) and l_{cz}:

$$l_e = \frac{l_{cz}}{N_e} \tag{2.4}$$

Another method to increase the convergence of the model is to lower the penalty stiffness of the element. This would result in a larger cohesive zone length and therefore more elements would be present in the cohesive zone or a larger mesh size can be adapted [46]. However, having a low value for the penalty stiffness can add artificial compliance to the model. Values that are often found in literature ranges from 10^5 to 10^8 N/mm^{-3} [47, 48].

Furthermore, when a cohesive element is fully damaged the energy release due to the stiffness of the element going to zero is often compensated with the use of viscoelastic regularization

in order to achieve convergence [49]. However, a high viscosity parameter can over predict the failure load [50].

Concluding, analyzing delamination or skin-stringer separation using cohesive elements is very useful, but experimental tests are necessary in order to validate if the cohesive elements behave correctly as the behavior depends on many nonstandard properties.

2.5 Global/Local Approach

To capture failure at ply level in a numerical model, complex elements with a fine mesh are needed. However, to capture the global behavior of a structure, the opposite is true. To find a balance between the two, Orifici et al. [51] used the global/local approach, which is a two step method that uses the results of the global behavior of a panel as input for a smaller sized specimen. The first step is to create a large structure, such as a multi-stringer panel in 2.18a, and apply a coarse mesh with shell elements. Loads and boundary conditions are applied after which an analysis is done on the model. A smaller local model is created, with a fine mesh, complex elements, such as brick elements, and including damage models, see 2.18b. The coordinate of the local model matches the global model and the results of the global model are used as an input for the boundary conditions of the local model. If the node of the local model does not match the position of a node on the global model, the results are interpolated. A subroutine was used to update the local model with the input of the global model until failure onset occurred. The global coordinates of the local model can than be shifted to a new location and the local analysis can be repeated. The global model does not have to be rerun every time a new local analysis is started. However, the drawback is that the failure onset that occurs in the local model is not copied to the global model and therefore the results of the global model are not representative anymore after the onset of delamination. This method is therefore best suited for finding the damage initiation. The local model that is created often corresponds to an actual experimental specimen, from which the results can later be verified.

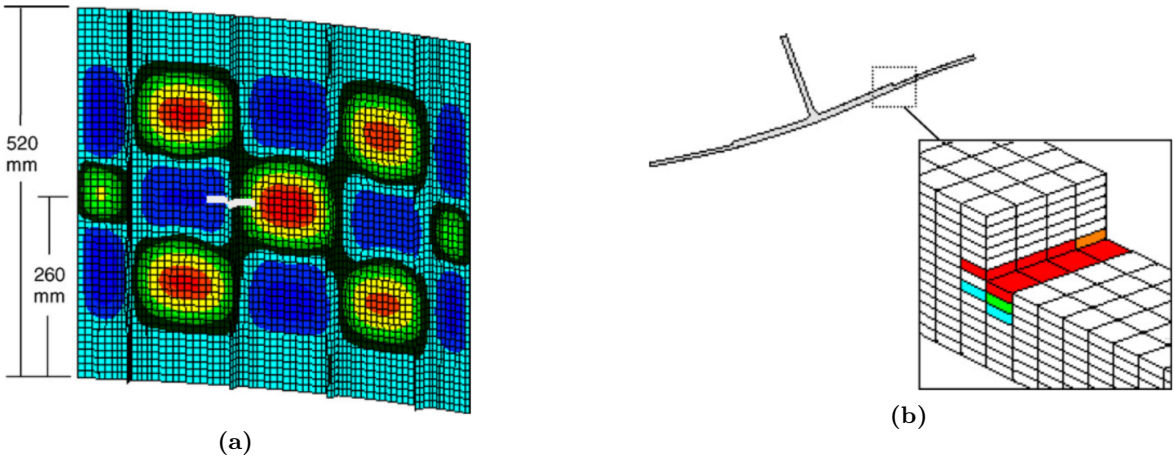

(a) (b)

Figure 2.18: Global/local analysis of Orifici et al. [51] showing a) the global model of a multi-stringer panel and the b) local model with brick elements.

Vescovini et al. [20] used the global/local approach on a five stringer panel as a global model. The local model was similar to a single-stringer compression specimen. Five local models were created on the middle stringer of the full panel, with the left and right boundary ending between the two stiffeners, which is shown in Figure 2.19. Four extra local models were used that overlapped the other five models in order to capture the effects that could occur at the boundaries of the initial five models. The models had a mesh size of 5 mm x 5 mm and 1 mm x 1 mm for the global and local model respectively. The response of the global panel was tied to the local panel using the integrated Abaqus submodel. Although the dimensions of the global and local model were different, the number of degrees of freedom of the FE model were approximately equal. The results of the global model focused on the out of plane displacement of the structure in postbuckling. The local model showed the delamination failure that occurred due to the interlaminar stresses that resulted from the postbuckling state of the structure. The global model took 2 hours to run and 3 hours for each local model, resulting in a 29 hours of total runtime.

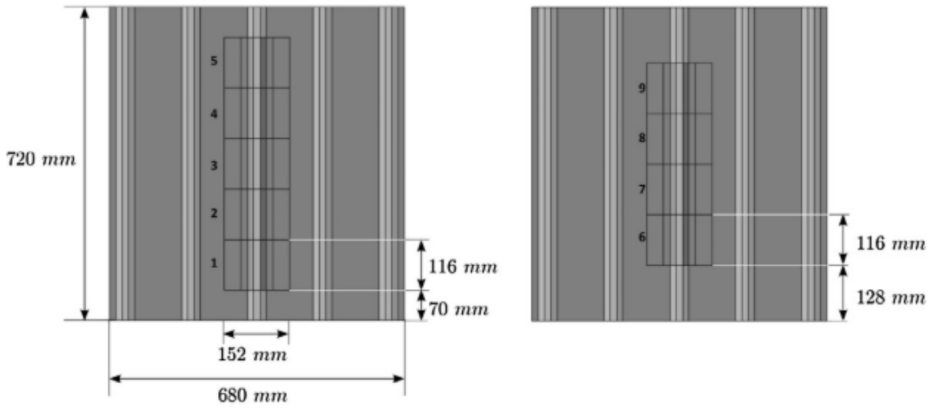

Figure 2.19: Global/local analysis of Vescovini et al. [20].

2.6 Research Question and Objective

The purpose of this literature study was to obtain knowledge on mode III delamination and postbuckling tests that are performed on the coupon and element level, respectively. A lack of research was observed in specifically the element level tests and from there the following research goals and questions can be formulated.

2.6.1 Research objective

The objective of this research is to create a methodology for the determination of an adaptive test configuration, which is able to characterize the skin-stringer separation that can occur in a postbuckled stiffened composite panel. The methodology that is described in this thesis is fully numerical using Abaqus as a FE software and Python for pre- and postprocessing.

The 7PB test was already able to capture the mode I + II opening that occurred at the maximum deformation of the buckling wave. The adaptive configuration should also be able

to capture other forms of crack initiation, such as the mode II + III opening at the inflection point of a buckling wave as seen by Vescovini et al. [20]. The number and location of the loading and support points will depend on the form of separation. The configurations are designed to be used for a single-stringer specimen at first, which has also been used in the research of the 7PB test by Bertolini et al. [6, 11] and of the SSC test by Bisagni, Dávila and Vescovini [13, 14, 20–22, 52].

2.6.2 Research question

The research question and sub-questions follow from the objective described in previous sub-section.

- What is the methodology to create a configuration that is adaptable to asses different regions of a postbuckled multi-stringer panel?
  - How does the behavior of single-stringer specimens in different loading conditions compare to the displacement field of a multi-stringer compression panel?
  - What kind of skin-stringer separation is seen in the multi-stringer compression panel?
  - What is the configuration needed to get a mode II + III separation at the inflection point?

Chapter 3

Four-Stringer Panel

Before exploring skin-stringer separation, the global buckling behavior of a multi-stringer panel has to be investigated. This chapter starts with Section 3.1 on the general description of the four-stringer panel FE model. Section 3.2 presents more insights into the different possible buckling modes of the panel. Different FE solvers are used to model the nonlinear buckling behavior of the panel under in-plane compressive loading, for both panels with and without an initial imperfection, as described in Section 3.2. On the panel without any imperfections, three distinct locations at which high deformation of the skin occurs are highlighted in Section 3.3.

3.1 Finite Element Model

A simplified version of the panel that is used in the NASA Advanced Composite Project [2] will be used in this research. This panel consists of a skin with four hat-stringers. The geometry and the dimensions of the panel and of the stringer are shown in Figures 3.1a and 3.1b, respectively. The width of the center bay, between the inner two stringers, is slightly larger than the outer bays. This is to induce a primary buckling mode in the center bay, ensuring that the skin-stringer separation will initiate at the stringer flange in the center bay. The skin and stringers in the simplified panel are made of graphite-epoxy IM7/977-3 [53], the properties of which are reported in Table 3.1. The stacking sequence for the skin and stringers is quasi-isotropic: [-45/45/0/90/-45/45]s. The resulting symmetric lay-up for the skin, the stringer and the skin-stringer overlap minimize the the residual stresses that develop during manufacturing.

The FE model of the four-stringer panel is developed in Abaqus 2017 [49] to investigate the out-of-plane deformation due to buckling. The skin and stringer are discretized using a 5 mm x 5 mm mesh that consists of four-noded conventional shell elements with reduced integration (S4R). These computationally efficient elements can capture the nonlinear response of thin structures subjected to large deformations. For this research, only compressive loading due to end-shortening of the panel is investigated. In the FE model, the skin and stringers are clamped at both sides of the panel to apply the end-shortening.

Table 3.1: Lamina properties of IM7/977-3.

t_{ply} (mm)	E_{11} (GPa)	E_{22} (GPa)	G_{12} (GPa)	G_{13} (GPa)	G_{23} (GPa)	ν_{12} (-)
0.127	164	9.0	5.0	5.0	3.0	0.32

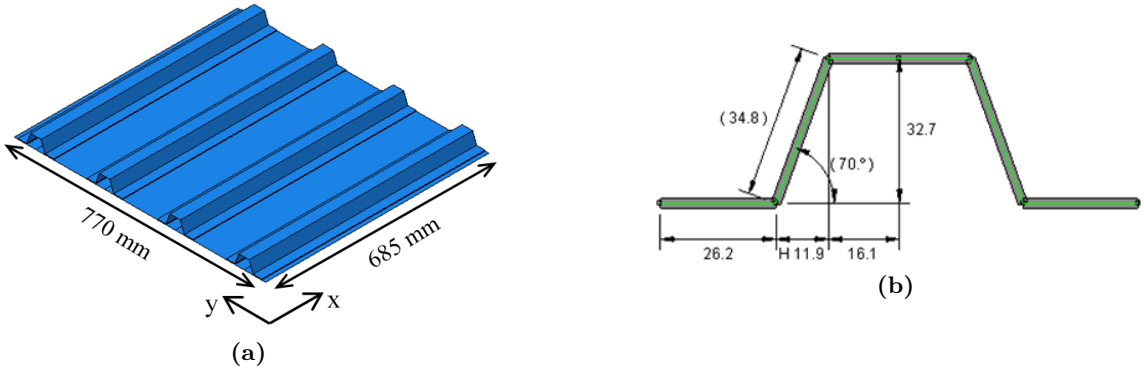

Figure 3.1: Geometry of a) the four-stringer panel and b) the hat-stringer with dimensions in mm.

3.2 Finite Element Analyses

The FE analysis of the four-stringer panel can be divided into two steps: Determining the eigenmodes of the panel using a linear buckling eigenvalue analysis and evaluating the effect of modal imperfections on the panel, when loaded in compression.

3.2.1 Buckling eigenvalue analysis

The deformation due to buckling of the panel can be investigated using an eigenvalue analysis. This allows to obtain the eigenvector and the corresponding eigenvalue of the panel. The eigenvectors consist of normalized displacement results, such that the maximum value in the vector is equal to one. Therefore the eigenvector only predicts the buckling shape of the structure and not the magnitude. The eigenvalue that corresponds to the eigenvector is equal to the buckling load or displacement, depending if the user applied a load or displacement of one as an input. The eigenvectors are calculated from the stiffness matrix of the panel. Therefore, the number of eigenvectors present in a FE model is equal to the number of degrees of freedom. However, only the eigenvectors with a low eigenvalue are of interest. The contour plot of the normalized out-of-plane displacement of the first four buckling modes are shown in Figures 3.2-3.5. The former two and latter two have similar eigenvalues. The corresponding displacement of these buckling eigenmodes is approximately 0.6 mm at a load equal to 100 kN.

For this four-stringer panel, the first four buckling modes show a buckling pattern of 4-6 buckling half-waves, primarily on the skin of the center bay. This is desired in order to

obtain skin-stringer separation at an interface in this mid-section. The number of buckling half-waves that are present on the skin might effect the type of skin-stringer separation that will occur in the panel. For example, the first buckling eigenmode shows five half-waves with an average length of approximately 135 mm. Whereas the average length of the half-waves for eigenmode 2 and 3 is approximately 115 mm. This would mean that for the same maximum out-of-plane displacement at the peak of a buckling half-wave, the twisting between the locations of minimum and maximum out-of-plane displacement increases with a decrease in wavelength.

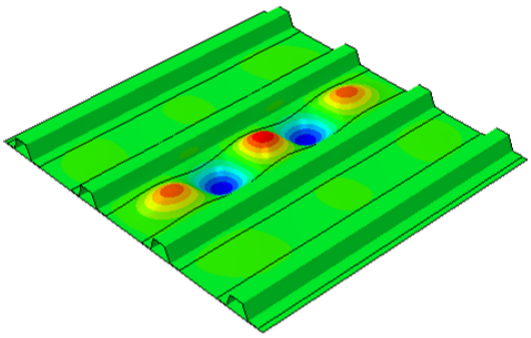

Figure 3.2: 1^{st} buckling eigenmode at a displacement of 0.59 mm and a corresponding buckling load of 96 kN.

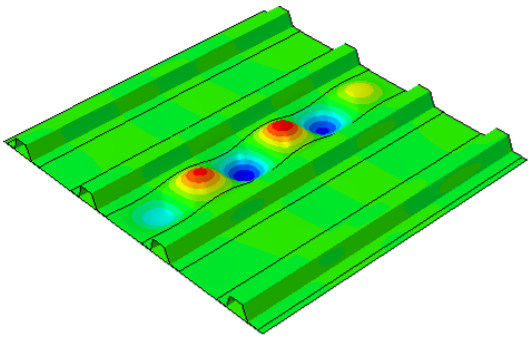

Figure 3.3: 2^{nd} buckling eigenmode at a displacement of 0.59 mm and a corresponding buckling load of 96 kN.

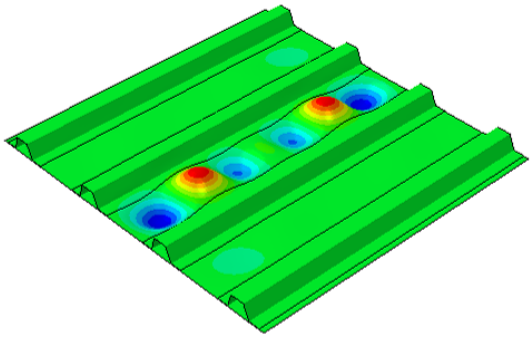

Figure 3.4: 3^{rd} buckling eigenmode at a displacement of 0.62 mm and a corresponding buckling load of 100 kN.

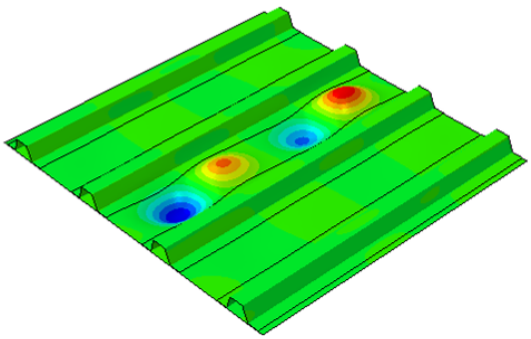

Figure 3.5: 4^{th} buckling eigenmode at a displacement of 0.62 mm and a corresponding buckling load of 100 kN.

3.2.2 Sensitivity of imperfections

As a first step, the FE model of the four-stringer panel without any imperfections is subjected to end-shortening up to a displacement of 5 mm. This applied displacement corresponds to an axial compression of 7300 microstrain, which is somewhat higher than the expected failure of the panel [2]. The panel shows a fully developed buckling deformation in all three skin bays at an end-shortening equal to 2 mm. Therefore, the results of this panel with the contour plot of out-of-plane displacement corresponding to an end-shortening of 2 mm is shown in Figure 3.7a.

Next, the four-stringer panel is also subjected to a sensitivity study to evaluate the effect of modal imperfections, where two comparisons are being made. The first comparison is done by applying different imperfection sizes of the same eigenmode to the panel. The first eigenmode is taken as the baseline with an imperfection of -0.1, 0.1 and 1 mm, shown in Figures 3.7b, 3.7c and 3.7d. The second comparison is made between the different eigenmodes: eigenmode 1, eigenmode 2 and eigenmode 3, with the same size of imperfection equal to 0.1 mm, shown in Figures 3.7b, 3.7e and 3.7f.

The force-displacement curves of all these models can be found in Figure 3.6. From these curves it can be observed that the type of imperfection or its size has little influence on the global stiffness of the panel. This can possibly be attributed to the fact that these eigenmodes primarily have a buckling wave in the central skin bay. Therefore, these buckling eigenmodes as imperfection only affects the four-stringer partially, leaving the outer bays unaffected. Also, the start of buckling is consistent over all models, which is expected as all eigenmodes occurred at an in-plane displacement of 0.6 mm.

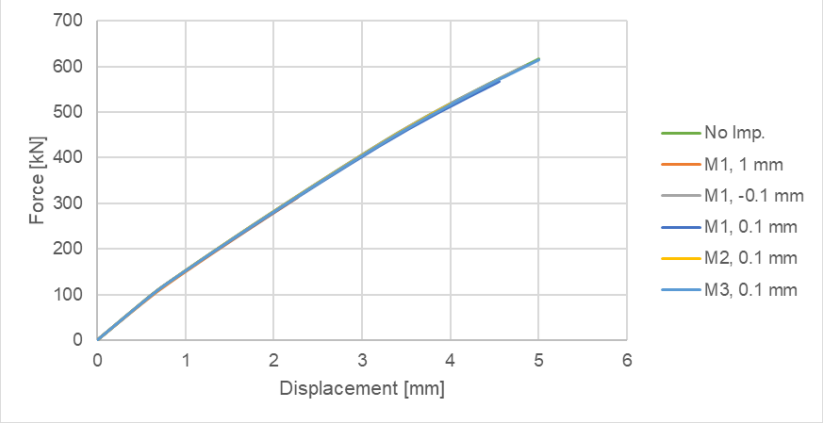

Figure 3.6: Quasi-static analysis of four-stringer panel force-displacement response.

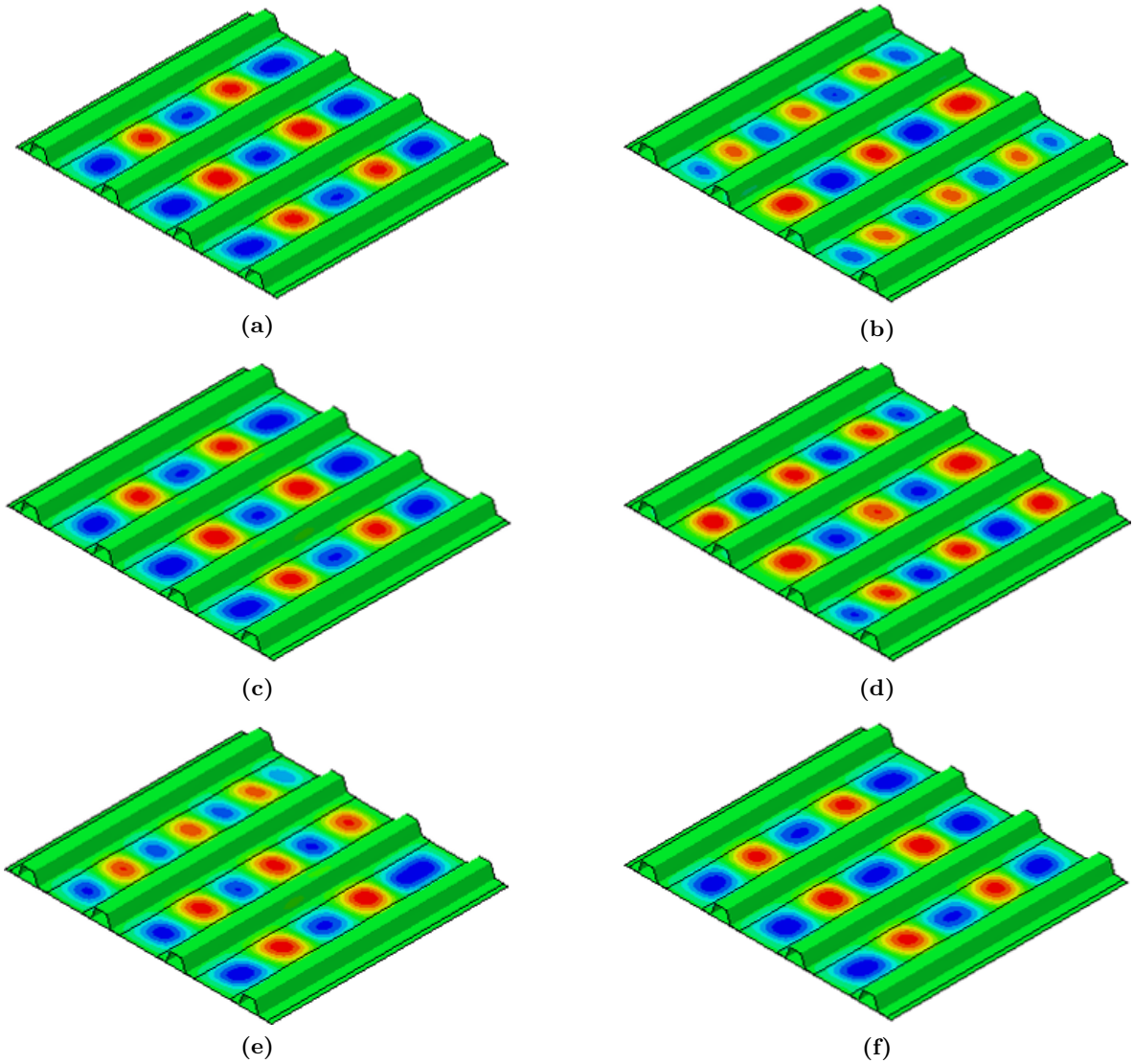

Figure 3.7: Quasi-static analysis of four-stringer panel, contour plot of out-of-plane displacement: a) without imperfections; b) mode 1 with an amplitude of 0.1 mm; c) reversed mode 1 with an amplitude of 0.1 mm; d) mode 1 with an amplitude of 1 mm; e) mode 2 with an amplitude of 0.1 mm; f) mode 3 with an amplitude of 0.1 mm.

3.3 Regions of Maximum Deformation

The goal of this thesis is to develop a numerical method to investigate possible skin-stringer separation in multi-stringer panels. The first step is to try and approximate the buckling behavior in certain regions of the panel using a representative single-stringer specimen. This method will be developed using the results of the four-stringer panel without any imperfections as the reference panel, which is shown in Figure 3.7a. In this panel three different regions can be identified: maximum displacement of the skin in positive z-direction, maximum displacement of the skin in negative z-direction and maximum twisting of the skin in between the other two regions.

3.3.1 Maximum +z displacement

The region of maximum skin displacement in positive z-direction will not be investigated. In this region the skin will deform towards the stringer flange, which will lead to a closing of the skin-stringer interface. Therefore only in-plane shear (mode II) is present, which makes this region not critical [51].

3.3.2 Maximum -z displacement

This region of the four-stringer panel encloses the maximum deformation of the skin at either side of the stringer. The large deformation of the skin promotes a combination of a dominant tensile opening of the interface (mode I) and in-plane shear (mode II). This could be a critical region in which the mode I-dominant opening can lead do skin-stringer separation.

3.3.3 Maximum twisting

This region encloses the inflection point of the buckling wave at each side of the stringer. This twisting deformation that occurs at the inflection point can result in skin-stringer separation due to a combined in-plane (mode II) and out-of-plane (mode III) shear. This type of shear dominated skin-stringer separation has received little attention [11, 20, 54], because a mode I opening at maximum -z displacement is often more dominant. However, this mode I opening is critical in a design where there is a high difference between the flexural stiffness of the skin and stringer layup, which leads to peel stresses at the termination of the stringer flange. The introduction of thinner flanges or ply drop-offs [11] that results in a tapered flange [6, 7, 51] can make the mode I opening less critical.

Chapter 4

Methodology

The two highlighted regions of the four-stringer panel without imperfections in Figure 4.1 show the maximum deformation (region 1) and maximum twisting (region 2) of the skin, which may cause separation of the skin-stringer interface. These two regions will be approximated using a FE model of a representative single-stringer specimen. This model is described in Section 4.1 as well as the Python tool that is used for pre- and post-processing of the results of the FE model. The methodology is applied to region 1 as discussed in Section 4.2 in which a 7PB configuration is used with variable positions of the supports and loading points to approximate the displacement field of this region. Region 2 is discussed in Section 4.3, where a ECT configuration is used to approximate the twisting behavior that is observed in this region. These sections describe the FE model, including the boundary conditions. The effect of the different loading conditions for such a configuration on the out-of-plane deformation is studied. Furthermore, the loading conditions that have the smallest error with respect to the corresponding region will be used to verify that these loading conditions are also valid at high postbuckling loads.

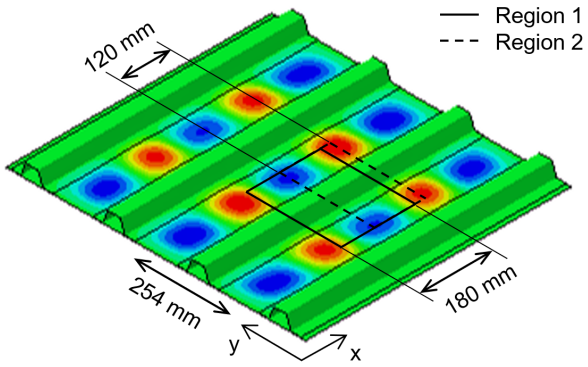

Figure 4.1: Out-of-plane displacement contour plot of four-stringer panel with the regions of maximum bending and twisting.

4.1 Methodology

The objective of the present work is to develop a methodology to design an experimental test that can be used to evaluate the different critical locations in postbuckled composite multi-stringer panels where skin-stringer separation may occur. The first goal of this effort is to develop specimens that can approximate the four-stringer panel response of these critical locations. The postbuckling deformation of a four-stringer panel is investigated and two critical regions of the panel are identified. Two specimens representing these critical locations are designed. The first one is representative of the region of the four-stringer panel with maximum out-of-plane skin deflection and the second one is representative of the region around an inflection point in the postbuckled deformation of the four-stringer panel. Different loading conditions of these configurations are obtained by varying the positions of the supports and loading points. The out-of-plane deformation of the specimen for each condition is compared to the shape of the postbuckling deformation of the corresponding region of the four-stringer panel.

4.1.1 Finite element model

The specimen that is used to approximate the regions of the four-stringer panel consists of a skin with a single hat-stringer. The skin and stringer are made of graphite-epoxy IM7/977-3, the properties of which are reported in Table 3.1. The stacking sequence for the skin and stringers is quasi-isotropic: [-45/45/0/90/-45/45]s. The length of the single-stringer specimens will be discussed in Section 4.2 for region 1 and in Section 4.3 for region 2 as it will be different for both configurations. The skin and stringer are discretized using a 2 mm x 2 mm mesh that consists of S4R elements. Each support will be modeled as boundary conditions applied to a single node by enforcing the out-of-plane displacement at that node to be zero. The loading point will be modeled as a boundary condition that enforces an out-of-plane displacement to a single node on the skin. Additional degrees of freedom are constrained for the loading points in order to prohibit any free body rotations of the specimen.

4.1.2 Overview of the methodology

The first step is to approximate the out-of-plane deformation of these critical locations using the FE model of a representative single-stringer specimen. The block diagram for this process is illustrated in Figure 4.2. This is done by defining different position for the supports and loading points on a single-stringer specimen in the 7PB and ECT configurations, which are discussed in Chapter 2. Different positions for the supports and loading points should result in a change in out-of-plane displacement field of the single-stringer specimen. For each loading condition, the out-of-plane displacement results are compared between the specimen and the corresponding region, from which the loading condition that leads to the smallest difference between these results is considered to be optimal. For this optimization procedure, a numerical tool is designed that combines the automatic pre- and post-processing capabilities of Python 3.6 with the FE solver of Abaqus 2017.

The Python tool defines an input file for every iteration, where in each iteration the position of the supports and/or loading points is adjusted. Hereafter, the tool submits the input

file as a job in Abaqus. After the analysis is finished, the tool extracts the nodal out-of-plane displacement data of the specimen and calculates the shape error with respect to the corresponding region of the four-stringer panel. These steps are repeated until the loading condition that yields the lowest shape error is found.

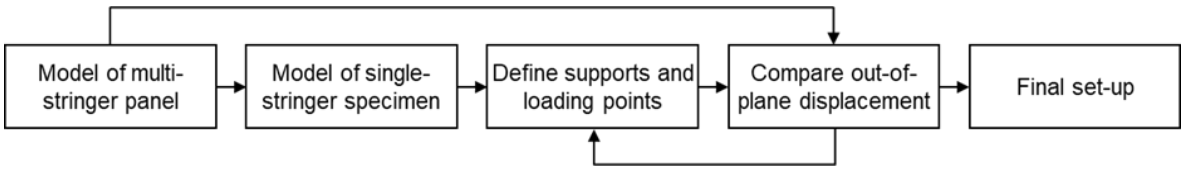

Figure 4.2: Block diagram for approximating the regions in the four-stringer panel.

4.1.3 Calculating the shape error

The out-of-plane displacements of the single-stringer specimen in the different loading conditions are compared with the out-of-plane displacement of the corresponding region of the four-stringer panel by calculating the residual sum of squares (RSS) [55]. The condition that results in the lowest RSS corresponds to the best approximation of the desired deformation. The equation for RSS is given by:

$$\mathrm{RSS} = \sum_{i=1}^{n} \left(y_i - f\left(x_i\right)\right)^2 \tag{4.1}$$

where y_i is the nodal out-of-plane displacement in the region of the multi-stringer panel. The approximation function f is a linear interpolation function of the out-of-plane displacement of the single-stringer specimen. This is done to overcome the problem of having a mismatch in mesh between the region of the four-stringer panel and the single-stringer specimen. Therefore $f(x_i)$ is the out-of-plane displacement of the single-stringer specimen that corresponds to the coordinates of y_i. Since the RSS is the sum of all squared differences, its value will increase for a decrease in mesh size.

4.2 Region 1

The configuration that will be used to approximate region 1 of the four-stringer panel is the 7PB configuration. Using five supports and two loading points, a shape similar to a buckling half-wave is induced on a single-stringer specimen. By altering the position of the supports and loading points, the out-of-plane deformation observed in the single-stringer specimen changes. By comparing the out-of-plane displacement results of different loading conditions to the deformation of region 1 of the four-stringer panel, the optimal loading condition can be found that minimizes the value of RSS. In order to verify if the loading conditions is valid for higher postbuckling loads, it is compared to the deformation of region 1 at a higher in-plane end-shortening, based on the expected failure of the panel.

4.2.1 Configuration

The out-of-plane deformation of region 1 in the four-stringer panel is approximated using a single-stringer specimen in a 7PB configuration, as illustrated in Figure 4.3. The boundary conditions consist of five lower supports and two upper loading points. The model is used to perform a parametric study to find the optimum loading condition of the 7PB configuration that best represents the deformation of the corresponding location on the four-stringer panel. The distances S_X and S_Y define the positions of the corner supports, and L_X and L_Y are the longitudinal and transverse distances to the edge of the skin that define the locations of the loading points. The following design constraints are imposed to the four position variables such that the configuration is defined by two independent variables, S_Y and L_Y:

- The corner supports and the loading points must be at least 20 mm away from the edges of the specimen to ensure that the stress concentrations at the free edge are limited ($S_X \geq 20$ mm, $S_Y \geq 20$ mm and $L_Y \geq 20$ mm).
- The corner supports and loading points are placed symmetrically along both axes ($L_X = 90$ mm).
- The distance S_X is taken equal to 20 mm, because this is the position of the inflection line between the half-waves in region 1 of the four-stringer panel. ($S_X = 20$ mm)
- The fifth support is positioned at the center of the specimen.

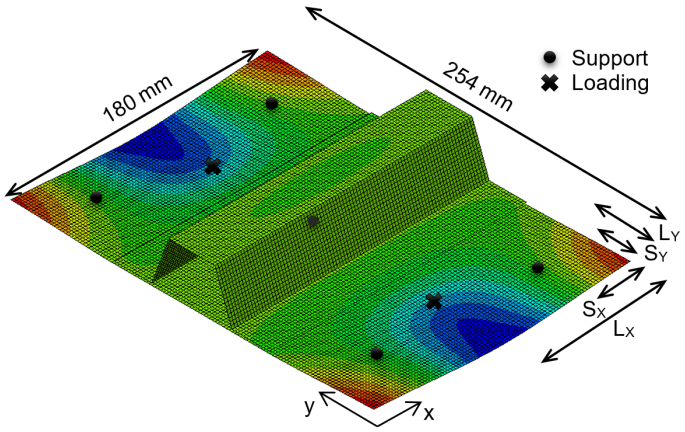

Figure 4.3: Seven point bending configuration.

The length of the buckling half wave observed in region 1 is approximately equal to 140 mm. The total length of the region is defined as the buckling half-wave length plus two times the minimum distance from the supports to the skin edge resulting in a total length of 180 mm. The width of the region is defined by the distance between the maximum deformation at one side of the stringer to the maximum deformation on the other side plus the additional 20 mm at either side of the specimen, which is approximately 250 mm in total. The specimens will be cut from a larger multi-stringer panel. The stringer spacing in this panel is 254 mm. To optimize the use of material in this panel, the width of all specimens will also be equal to 254 mm. The final length by width of region 1 in the four-stringer panel and of the 7PB specimen is 180 mm x 254 mm. Although the size of the single-stringer specimen is 254 mm x 180 mm, only the relevant area of this specimen, defined by $20 \leq x \leq 160$ and $20 \leq y \leq 234$, will be compared to the corresponding region 1 of the four-stringer panel.

4.2.2 Loading conditions

For the 7PB configuration, the RSS surface is plotted as a function of the variables S_Y and L_Y in Figure 4.4. From this plot it can be seen that there is a tendency of having a low RSS, when the loading point is positioned slightly further from the edge than the supports. Furthermore, positioning the loading points closer to the edge often leads to a decrease in RSS. The change in RSS as a function of variables S_Y and L_Y becomes smaller near the loading conditions that leads to the minimum value of RSS. For this configuration, the loading conditions with $S_Y = 20$ mm and $L_Y = 34$ mm leads to the lowest shape error, when compared to region 1 of the four-stringer panel.

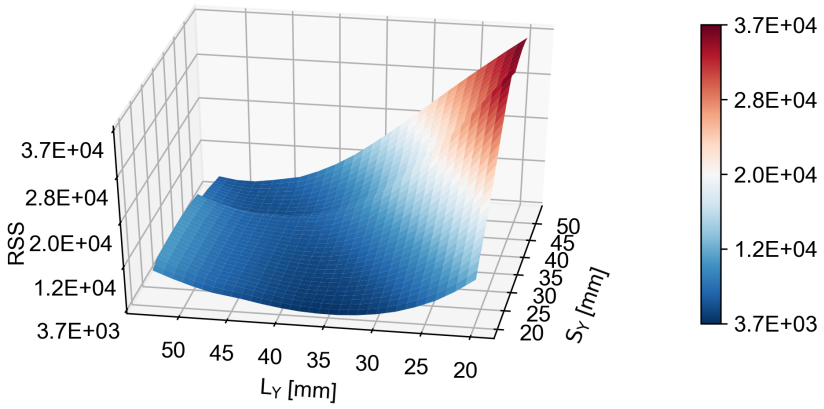

Figure 4.4: Surface plot of RSS for region 1 as function of variables S_Y and L_Y.

The out-of-plane displacement for region 1 is shown in Figures 4.5a and 4.5b together with the results for the 7PB specimen for six different sets of values of the variables S_Y and L_Y. These figures show a darkened area at the edge of the plot, this area is not taken into account for the calculation of the value of RSS. When comparing these six different loading conditions, some trends can be observed that explain the behavior observed in Figure 4.4. Increasing L_Y results in a higher gradient of the deformation between the flange and the loading point, but it decreases the gradient between the loading point and the free edge of the specimen. Increasing S_Y results in a wider buckling wave towards the edge of the skin. This is observed when comparing the loading conditions of $S_Y = 20$ mm and $L_Y = 20$ mm to the condition where $S_Y = 34$ mm and $L_Y = 20$ mm. From Figure 4.4, it is observed that the difference in RSS between the loading conditions where $S_Y = 20$ mm and $L_Y = 34$ mm and the condition where $S_Y = 34$ mm and $L_Y = 34$ mm is relatively small, which is also observed when these plots are compared. For the condition $S_Y = 20$ mm and $L_Y = 34$ mm, the value of RSS is minimum. The applied transverse displacement at the loading points for this loading conditions is 3.8 mm, which corresponds to a total loading force of 800 N.

Some of the observations that were made can be further backed by viewing the corresponding force-displacement response in Figure 4.6. For example, increasing S_Y results in a wider buckling wave towards the edge of the skin, which can be attributed to the fact that there is less limitation on the deformation when the supports are placed closer to the center of the specimen. Therefore, the applied loading, to achieve the same out-of-plane deformation at the same point ($L_Y = 52$ mm), requires 1.5 times the force when changing S_Y from 20 mm to 52 mm. In addition, the change of L_Y leads a reduction in maximum applied displacement.

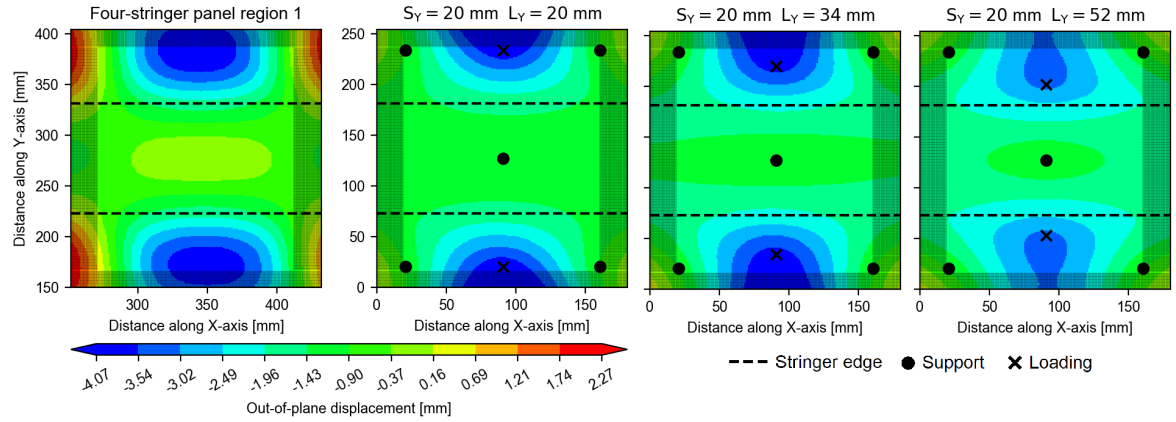

(a)

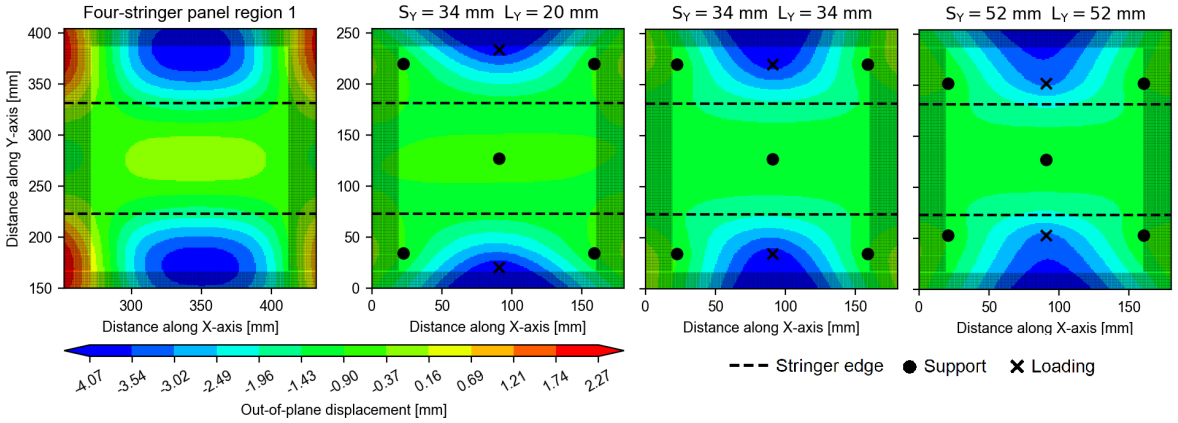

(b)

Figure 4.5: Contour plots of the skin out-of-plane displacement at an applied in-plane displacement equal to 2 mm for region 1 of the four-stringer panel and for six different configurations of the 7PB specimen. The effect of the transverse position of a) the loading points and b) the supports.

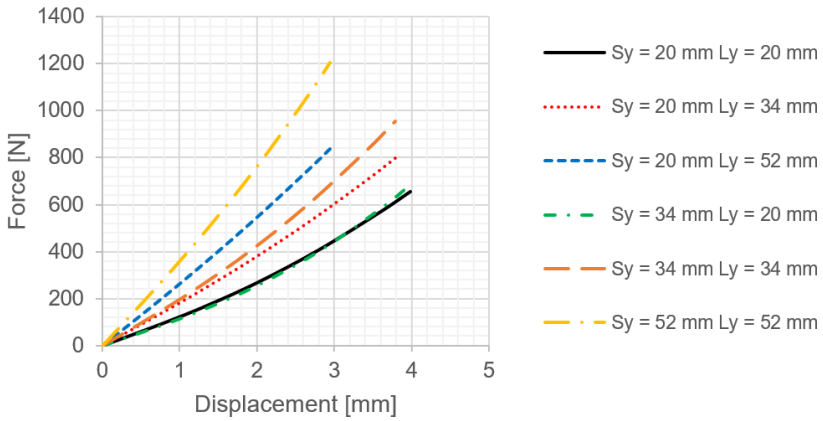

Figure 4.6: Out-of-plane force-displacement curve for the different 7PB loading conditions.

4.2.3 Deep postbuckling

To verify whether this configuration can still be used to approximate the deformation in region 1 at a higher in-plane compressive displacement of the four-stringer panel, a second comparison is performed at an applied in-plane displacement of 5 mm. The deformation shapes for both region 1 and the 7PB configuration are shown in Figure 4.7. Since no mode changes of the skin between the stringers takes place in the four-stringer panel between the applied in-plane displacements of 2 mm and 5 mm, the configuration of 7PB remains representative of the response of region 1 of the panel between the onset of debonding (applied displacement of 2 mm) and expected failure (applied displacement equal to 5 mm) [2].

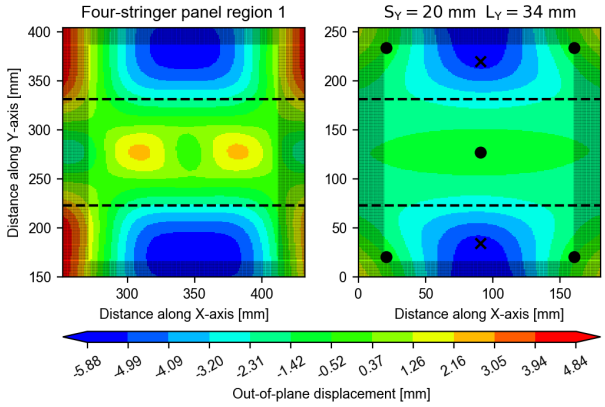

Figure 4.7: Contour plots of the skin out-of-plane displacement at an applied in-plane displacement equal to 5 mm: for region 1 of the four-stringer panel and for the 7PB specimen.

4.3 Region 2

In order to approximate the deformation field observed in region 2 of the four-stringer panel, an ECT configuration will be used. The ECT configuration uses two supports and two loading points, placed diagonally from each other, to obtain a twisting deformation. By altering the longitudinal and transverse position of these supports and loading points, the resulting out-of-plane deformation is changed. The optimal loading conditions results in the smallest shape error compared to the deformation of region 2.

4.3.1 Configuration

The twisting deformation of region 2 in the four-stringer panel is approximated using a single-stringer specimen in an ECT configuration, where two lower supports and two upper loading points, positioned diagonally from each other, were used to apply torsion to the specimen, as illustrated in Figure 4.8. A model of a single-stringer specimen is constructed with S4R elements. The variables for the ECT configuration are S_X and S_Y for the position of the supports and L_X and L_Y for the position of the loading points. The number of variables is reduced by imposing the following constraints to the configuration, leaving it with the two independent variables S_X and S_Y:

- The loading points and the supports are equidistant from the free edges ($S_X = L_X$ and $S_Y = L_Y$)
- The distance between the loading points to the free edges of the specimen must be greater than 20 mm ($S_X \geq 20$ mm and $S_Y \geq 20$ mm)

There is no fixed longitudinal position for the supports as opposed to the 7PB configuration and therefore the length of the specimen will be equal to the buckling half-wave length of region 2. This buckling half wave is taken from the maximum negative z-displacement at the center of the four-stringer panel to the adjacent maximum positive z-displacement. This length equals 120 mm. To minimize the loss of material during cutting of the specimens from a larger multi-stringer panel, the width of the specimen will be 254 mm, which is equal to the width of the single-stringer specimen of the 7PB configuration. When the four-stringer panel out-of-plane deformation field in postbuckling is anti-symmetric over the longitudinal axis with respect to the stringer, the area that is defined by $0 \leq x \leq 120$ and $20 \leq y \leq 234$ will be compared to the corresponding region 2 of the four-stringer panel. However, the postbuckling behavior in region 2 of the four-stringer panel, that is shown in Figure 4.1, resulted in a symmetric out-of-plane deformation with respect to the longitudinal stringer axis. Whereas the single-stringer specimen loaded in an ECT configuration will always lead to an anti-symmetric deformation field, because the specimen is twisted. In this case the area that is defined by $0 \leq x \leq 120$ and $127 \leq y \leq 234$ is used when the RSS is calculated with respect to region 2 of the four-stringer panel.

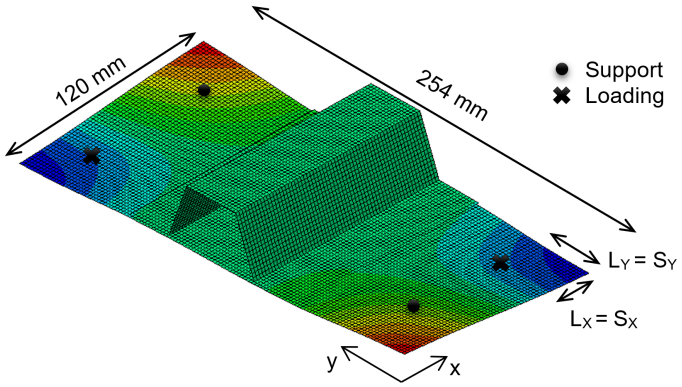

Figure 4.8: ECT test configuration.

4.3.2 Loading conditions

The postbuckling deformation in region 2 of the four-stringer panel is symmetric with respect to the longitudinal axis, whereas the ECT test configuration imposes an anti-symmetric deformation with respect to the longitudinal stringer axis. Therefore, the response of only half of the ECT specimen is compared against the corresponding region in the four-stringer panel. The RSS surface as a function of variables S_X and S_Y is plotted in Figure 4.9. For this configuration there is a clear minimum RSS that corresponds to a loading condition of $S_X = 30$ mm and $S_Y = 48$ mm. It can also be seen that the increase of S_X will often lead to an increase in RSS.

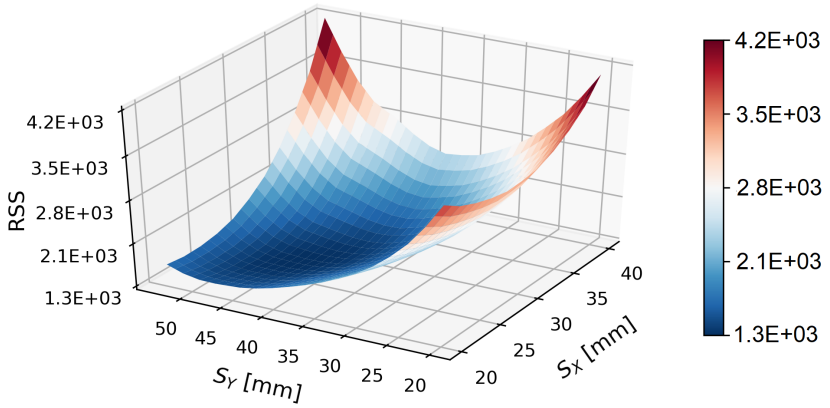

Figure 4.9: Surface plot of RSS for region 2 as a function of variables S_Y and S_X.

The out-of-plane deformation of region 2 in the four-stringer panel is compared in Figure 4.10 to the out-of-plane displacement of the single-stringer specimen with six different conditions of the ECT configuration. The darkened area at the bottom and top of the figure, from $y < 127$ mm and $y > 234$ mm, is not taken into account for the calculation of RSS. Increasing S_Y causes a higher gradient in the out-of-plane displacement between the stringer flange and the loading point. Increasing S_X results in a higher gradient between the support and loading point. From these iterations, the configuration with $S_X = 30$ mm and $S_Y = 48$ mm resulted in the lowest RSS. In this loading condition, the displacement of the two loading points is 4.2 mm, which corresponds to a total applied force of 920 N.

In Figure 4.11 the out-of-plane force-displacement responses of the ECT loading conditions shown in Figure 4.10 are plotted. The maximum displacement of the specimen in this ECT configuration is observed at a corner of the skin. Therefore, an increase in either S_Y or S_X will naturally result in a lower applied nodal displacement. In contrast to the response of the 7PB configuration, the force of the loading points and supports increases, when the supports and loading points are placed closer to the midpoint of the specimen. This can be attributed to the fact that the hat-stringer is the main contributor to the torsional rigidity of the specimen. If the supports are moving closer to the stringer, the moment arm becomes smaller and a higher force is needed to create a similar torsional behavior.

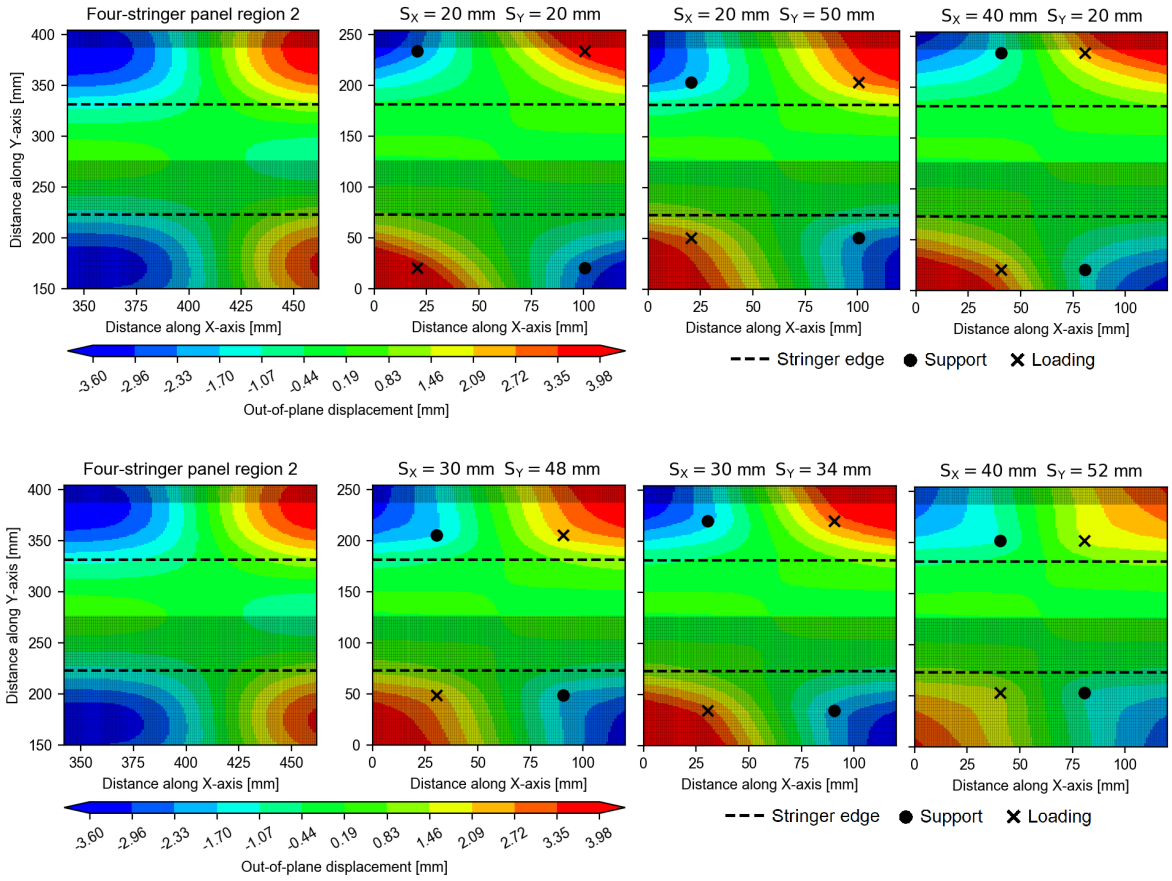

Figure 4.10: Contour plots of the skin out-of-plane displacement at an applied in-plane displacement equal to 2 mm for region 2 of the four-stringer panel and for six different ECT configurations.

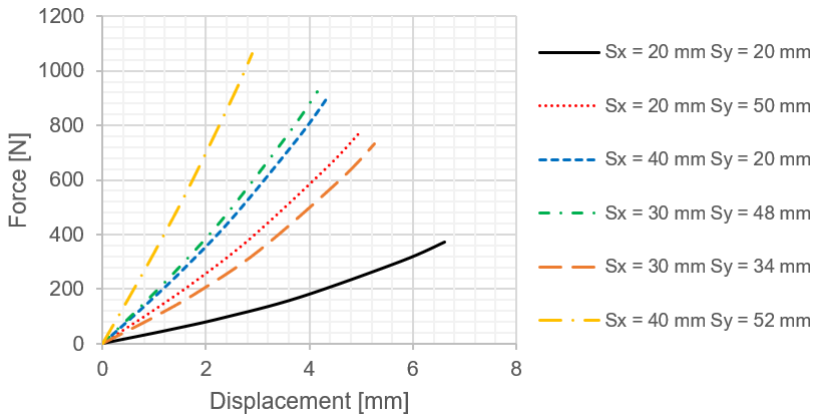

Figure 4.11: Out-of-plane force-displacement curve for the different ECT loading conditions.

4.3.3 Deep postbuckling

To verify whether this configuration can be used to represent the deformation of region 2 of the four-stringer panel at a higher applied in-plane compressive displacement, the analyses were repeated with an in-plane displacement equal to 5 mm. The deformation shapes for region 2 and the ECT configuration are shown in Figure 4.12. Since no buckling mode changes occur in the four-stringer panel between the onset of buckling at an applied displacement of 2 mm and expected failure with an axial compression of 7300 microstrain (applied displacement of 5 mm), the configuration of the ECT remains somewhat representative of the response of region 2 of the four-stringer panel. However, it must be noted that the increase in deformation gradient along the y-axis between the 2 mm and 5 mm in-plane displacement for region 2 of the four-stringer panel is too large for the ECT configuration to approximate.

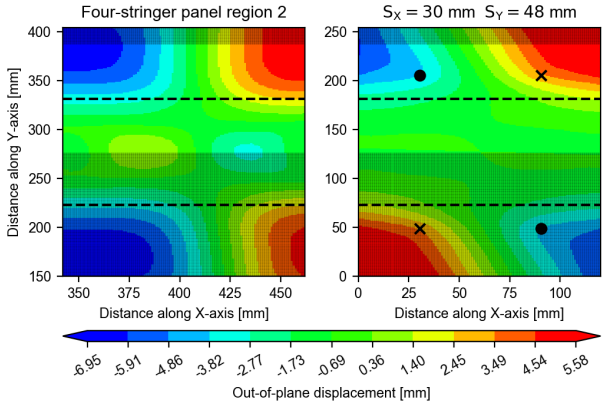

Figure 4.12: Contour plots of the skin out-of-plane displacement at an applied in-plane displacement equal to 5 mm: for region 2 of the four-stringer panel and of the ECT single-stringer specimen.

4.4 Concluding Remarks

This section presents the conclusion of this chapter. In addition, it presents some potential improvements for the Python tool that is designed for this first step of the methodology.

4.4.1 Conclusions

This chapter describes the first steps of a methodology that is under development for the study of the skin-stringer separation in postbuckled composite stiffened structures using single-stringer specimens. The buckling deformation of a four-stringer panel loaded in compression was analyzed and two critical deformation regions were identified. The first region, where the out-of-plane deformation of the skin is at its maximum, was approximated with the use of single-stringer specimen in a seven point bending configuration, in which five supports and two loadings points impose an out-of-plane deformation. The second region, characterized by twisting of the skin, was approximated using an edge crack torsion configuration, in which

two supports and two loading points apply out-of-plane displacements. The optimal position of the supports and loading points for these configurations were determined by minimizing the difference between the out-of-plane displacement of the single-stringer configurations and the out-of-plane displacement in corresponding regions in the four-stringer panel.

In Chapter 5, these optimal configurations will be applied to a more complex FE model in which skin-stringer separation can be simulated. The development of skin-stringer interlaminar damage will be investigated using a cohesive-based model.

4.4.2 Further improvements of the Python tool

Although the current state of the Python tool that is discussed in this chapter is sufficient for the research purpose in this thesis, further development is needed in order to obtain an efficient tool that is fit for general use. Some examples can be found below.

The current optimization tool evaluates all options within its boundary conditions. For the purpose of this research, this method was needed in order to visualize the error as a function of the supports and loading points in Figures 4.4 and 4.9. The total time for these models that use a mesh size of 2 mm x 2 mm, which resulted in approximately 200 different loading conditions for each configuration, was less than three hours. However, if more variables are added to this process an optimization algorithm is needed to reduce the computational time.

Some additional variables were considered for this process, but constrained using the design criteria that were discussed in Sections 4.2 and 4.3 in order to reduce the computational effort. Currently, the length of the specimen is calculated from the total buckling wave length plus additional overhang length to reduce any edge effects. However, having the length and width of the specimen as variables can also contribute in a more accurate approximation of the deformation field of critical regions of the four-stringer panel. Additionally, having continuous variables for the position of the loading points and supports can result in a more accurate optimal loading condition.

In addition, extra variables for the supports and loading points can be added to the optimization problem. For example, if the buckling pattern in a four-stringer panel is skewed. Bertolini et al. [11] have used the 7PB configuration in which the supports and loading points were positioned anti-symmetric with respect to the longitudinal and transverse midplane, which is shown in Figure 2.8d. This would already require an additional variable for the longitudinal position of the loading point. For even more irregular buckling shapes, potentially the position of all supports and loading points could be independent variables.

Chapter 5

Skin-Stringer Separation

The optimal loading conditions for a single-stringer specimen in the 7PB and ECT configurations were designed to minimize the difference in out-of-plane displacement between the four-stringer panel and the specimen. In order to verify that the specimen in such a loading conditions will also result in similar damage initiation behavior as would occur in the four-stringer panel, complex FE models are designed that use a cohesive damage model to simulate interface damage. The chapter will start with the investigation into damage initiation in the two regions of the four-stringer panel using a global/local analysis. Next, a description is presented in Section 5.2 of a Python tool designed to create input files for Abaqus that define a FE model including the cohesive zone damage model. The tool also allows to define the loading conditions of the configurations that were discussed in Chapter 4, which will be applied to a FE model that allows for skin-stringer separation. Section 5.3 describes region 1, which is approximated with a 7PB configuration. Section 5.4 describes region 2, which is approximated using an ECT configuration.

5.1 Damage Initiation in the Regions of the Four-Stringer Panel.

The global/local analysis is used to decouple the global buckling behavior of the four-stringer panel from the damage mechanisms in a local model. Two local models are created to study the damage initiation that can occur in region 1 and region 2 of the panel. First, the numerical models will be described in which cohesive elements are implemented to allow for damage. Next, the damage initiation that occurs in region 1 and in region 2 will be discussed.

5.1.1 Finite element model

The width and length of the region 1 local model is 254 mm x 180 mm and of the region 2 local model it is 254 mm x 120 mm. The stringer cross-section is shown in Figure 3.1b. The skin and stringers are made of graphite-epoxy IM7/977-3, the properties of which are reported in

Table 3.1. The stacking sequence for the skin and stringers is quasi-isotropic: [-45/45/0/90/-45/45]s. The properties of the cohesive interface between the skin and stringers are reported in Table 5.1 [2]. Due to the availability of the cohesive properties of IM7/8552 [2], these were used instead of the interfacial properties of IM7/977-3 [53]. This should not have a great influence as the properties are assumed to be rather similar.

Table 5.1: Interface properties of IM7/8552 for cohesive elements.

G_{Ic}	G_{IIc}	σ_c	τ_c	K_I	K_{sh}	η_{BK}
(Nmm^{-1})	(Nmm^{-1})	(Nmm^{-2})	(Nmm^{-2})	(Nmm^{-3})	(Nmm^{-3})	(-)
0.256	0.65	80.1	97.6	$4.76E5$	$2.29E5$	2.07

The FE models consist of SC8R elements, which are modeled with the actual thickness of the specimen. The thickness of the skin and stringer is 1.524 mm. The maximum element size in the mesh of the FE models is equal to 1.5 mm x 1.5 mm near the free edge of the specimen. The minimum mesh size at the location where the initiation of skin-stringer separation is expected is calculated with the equations discussed in Section 2.4 and this is equal to 0.17 mm. x 0.17 mm. In total, the FE model of region 1 consists of 800.000 nodes and 500.000 elements and of region 2 consists of 900.000 nodes and 600.000 elements.

The boundary conditions that are applied to the local models are taken from the results of the four-stringer panel model using the Abaqus submodelling technique [49]. For every displacement increment in the four-stringer panel, the resulting deformation at the nodes that are highlighted in Figures 5.1a and 5.1c are used as an input for the boundary conditions of the local model at the nodes that are highlighted in Figures 5.1b and 5.1d, for region 1 an region 2 respectively. Therefore, the damage initiation can be investigated in these two local models using the actual buckling deformation from the larger four-stringer panel. Using this method, the end-shortening of the panel at which damage initiation would occur in region 1 and in region 2 can be found.

The four-stringer panel without imperfections that is described in Chapter 3 is taken as the global model and the results from this panel from 0 to 5 mm end-shortening are used as input for the local models. This allows to find the in-plane compressive displacement of global model at which damage onset and initiation occurs in the local model. Damage onset is defined as the moment that the stiffness of the first cohesive element starts to degrade, which is when the quadratic stress criterion is met, explained in Section 2.4. When the stiffness of the first cohesive element is zero, which is when the damage parameter D is equal to one as explained in Section 2.4, the damage initiates. If more cohesive elements reach D = 1, the crack is propagating.

Using this method, the complex skin-stringer separation can be modeled with the fine mesh of the local model, whilst having the correct buckling out-of-plane response from the global model. However, the local model will undergo a loss of stiffness when the cohesive elements are damaged. This loss of stiffness is not communicated back to the global model, because this model does not allow any damage. There have been some authors that update the stiffness matrix of the global model based on the results obtained from the local model [56], but this method requires an iterative loop instead of a decoupled global/local model rendering it more

computationally heavy. The decoupled global/local model that is used here is therefore only used to investigate the damage initiation, as until that point minimal loss of stiffness has occurred and the results should be representative.

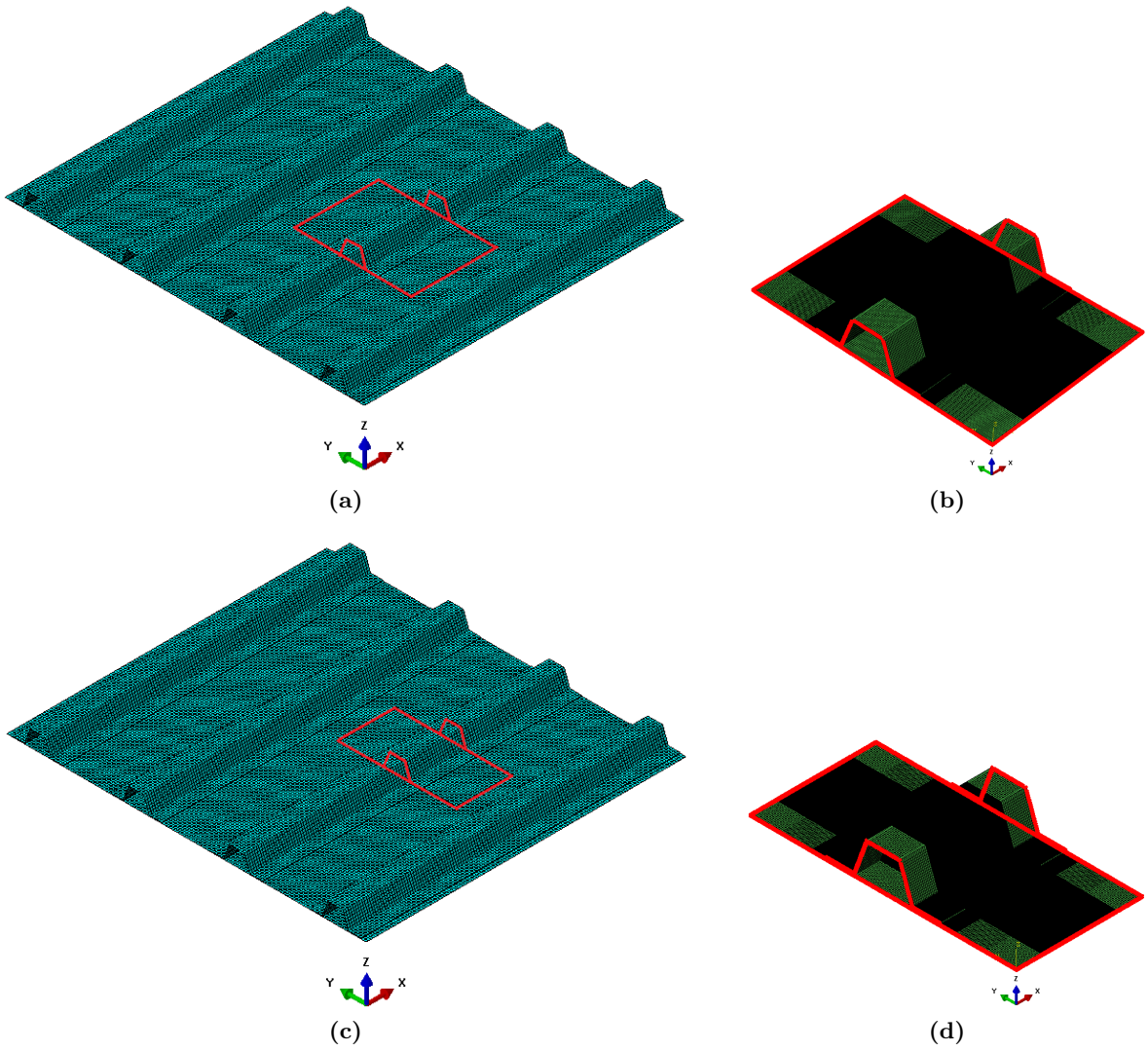

Figure 5.1: Global/local boundary conditions. a and c) Nodes of region 1 and region 2 of the global model used for b and d) the nodes of region 1 and region 2 local models at which the boundary conditions are applied.

5.1.2 Region 1

The damage initiation in the local model of region 1 is investigated, where a mode I opening is expected at the location of maximum deformation. The deformation of this model is shown in Figure 5.2 at an end-shortening of the panel of 2.0 mm. The deformation field of this local model is the same as the deformation in the highlighted region 1 in Figure 4.1, which is the

purpose of the global/local analysis. Also the cohesive zone at the skin-stringer interface is shown in Figure 5.2, highlighting the location of damage onset in the first cohesive element.

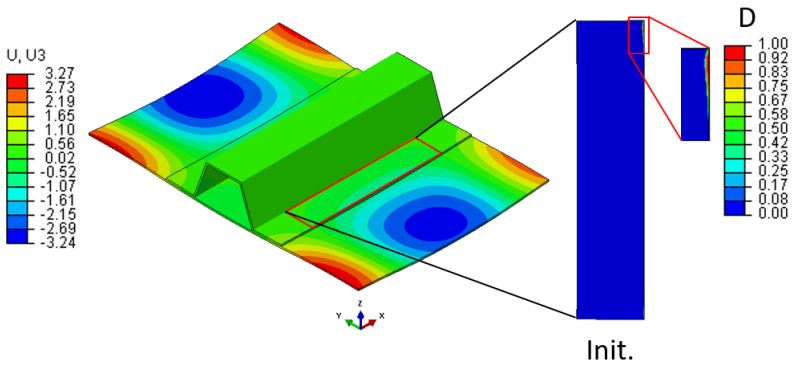

Figure 5.2: Damage initiation for region 1 in global/local analysis.

The location of damage onset is not at the maximum deformation of the buckling wave, but at the inflection point. Although the local model shows damage onset, the deformation needed for initiation is not reached. This is because there are no cohesive elements at the interface near the free edges of the stringer, which is shown in Figure 5.2. Instead, the skin nodes are rigidly tied to the stringer such that no damage can occur near the free edges due to any edge effects. Therefore, the rigid link between the skin and stringer nodes do not allow the already partially damaged cohesive elements to become fully damaged prior to an end-shortening of 5 mm.

The location of damage onset can possibly be attributed to the lack of mismatch in bending stiffness between the skin and the stringer. However, there are more locations in the four-stringer panel at which the displacement of a buckling half-wave is maximum. These other locations have to be investigated further to see if a mode I-dominant damage initiation occurs that can lead to skin-stringer separation. Furthermore, it should be investigated if initial damage present near the location of maximum displacement leads to a mode I opening of the interface. This can be studied by modeling the presence of a Teflon insert at the skin-stringer interface.

5.1.3 Region 2

Damage initiation in region 2 of the four-stringer panel is expected to start at the inflection point of the buckling wave. The deformation of the second local model at an in-plane displacement of 2 mm is shown in Figure 5.4, which is equal to the deformation observed in region 2 in Figure 4.1. The cohesive elements at the skin-stringer interface show damage onset at an in-plane displacement equal to 1.2 mm, shown in the force-displacement curve of the full panel in Figure 5.3. Damage initiates at an end-shortening of 3.5 mm, where the location of damage initiation is presented in Figure 5.4.

The postbuckling deformation of the four-stringer panel is investigated up to an end-shortening of 5 mm in Section 3. However further propagation of the crack is not investigated as the loss of stiffness that occurs in the local model is not communicated back to the global model.

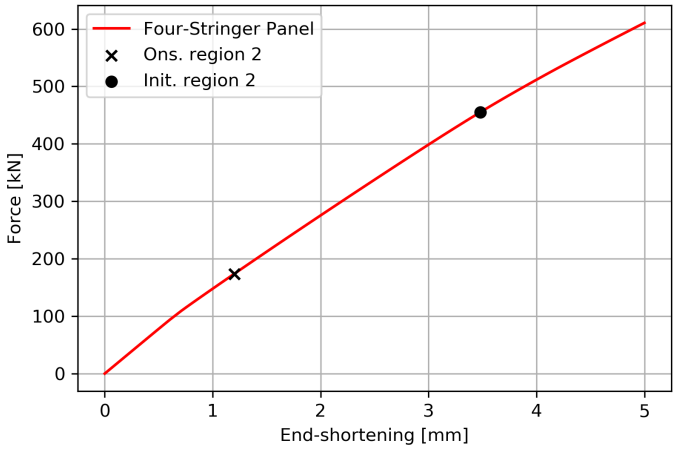

Figure 5.3: Force-displacement response showing damage onset and initiation in the local model of region 2.

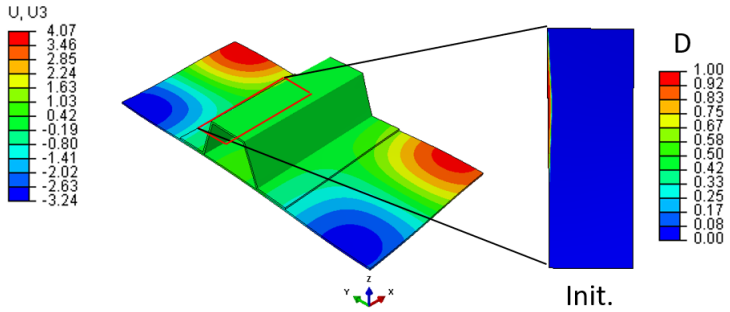

Figure 5.4: Damage initiation for region 2 in global/local analysis.

However, the location of damage initiation and the corresponding displacement of the skin nodes can be compared to a single-stringer specimen in am ECT configuration.

5.2 Python Tool to Create an Abaqus Input File

Creating FE models using the Abaqus GUI has limited options in the implementation of cohesive elements. Moreover, as this research focuses on the effect of positioning of supports and loading points, multiple different FE models of a single-stringer specimen are needed. In addition, the parameters that are used for the cohesive zone model can affect the initiation and propagation of the skin-stringer separation. Therefore, a Python tool is created that allows to change certain parameters such as the position of the supports and loading points and the parameters of the cohesive zone to create a new FE model. This tool is divided in dependent blocks, which are shown in Figure 5.5, and each of these blocks with its input and outputs will be discussed.

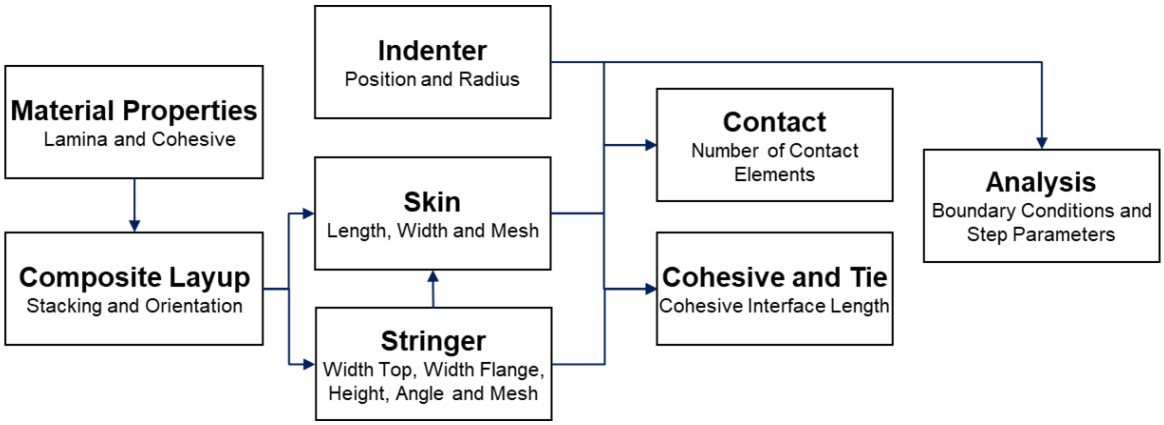

Figure 5.5: Block diagram for Python input file tool.

5.2.1 Material properties and composite layup

Lamina material properties The skin and stringers are both simulated using a composite layup, which receives the input from the lamina material properties . The Python tool allows to create a material database for lamina. In this database the following properties can be specified:

- Material name: Name for the database input
- t_{ply}: Thickness of a single ply
- E_{11}: Young's modulus in the longitudinal direction of the fiber
- E_{22}: Young's modulus in the transverse direction of the fiber
- G_{12}: In-plane shear modulus
- G_{13}: Out-of-plane shear modulus in 13 direction
- G_{23}: Out-of-plane shear modulus in 23 direction
- ν_{12}: In-plane Poisson ratio
- ρ: Density of the material

Composite layup The following items are used as the input of the composite layup block. All these inputs are defined separately for the layup of the skin and of the stringer.

- Ply orientations: List containing the orientation of every ply
- Ply material: List containing the material name of every ply
- Symmetric: Allows to define half of the layup and make it symmetric over the midplane

Cohesive material properties The skin-stringer interface is modeled using cohesive elements with a bilinear law as discussed in Section 2.4. The material properties that are used in the Python code can be found below:

- Cohesive Property Name: Name for the database input
- K_I: Penalty stiffness for mode I loading
- K_{sh}: Penalty stiffness for mode II and mode III shear loading
- G_{Ic}: Critical energy release rate for mode I
- G_{IIc}: Critical energy release rate for mode II and mode III

- σ_c: Maximum normal traction of the cohesive elements
- τ_c: Maximum shear traction of the cohesive elements
- η_{BK}: Benzeggagh-Kenane parameter

5.2.2 Skin and stringer

Skin The thickness of the skin is determined from the sum of the thickness of every lamina in the composite layup, the only two remaining parameters for the skin are the following:

- L_{sk}: Length of the skin
- W_{sk}: Width of the skin

Stringer The thickness of the stringer is determined from the sum of the thickness of every lamina in the composite layup and the length of the stringer is equal to the length of the skin. This leaves the remaining cross-sectional geometry as an input:

- H_{str}: Height of stringer from the mid-plane of the flange to the midplane of the top
- W_{top}: Width of the top of the stringer
- W_{fla}: Width of one flange of the stringer
- α_{str}: Outer angle between the flange and web of the stringer

Mesh The skin and stringer of this model are meshed using eight-noded continuum shell elements with reduced integration (SC8R). For the skin and stringer each, only a single layer of SC8R elements is currently used. However using more elements through-the-thickness should improve the transverse shear response, but also increases the size of the model. Care is taken to orient the stacking direction of these elements correctly, especially at the webs of the stringer, to make sure that the thickness direction of the composite layup matches the thickness direction of the shell element. Also, the SC8R elements are modeled using a finite thickness, which can be used to model the contact constraints at either side of the elements for the supports and loading points [49]. The finite thickness is also useful for creating zero-thickness cohesive elements by sharing the top nodes of the skin and bottom nodes of the stringer at the interface. The surfaces of each element in the mesh that is created in this tool are rectangular, except for the elements that are positioned at the corners of the stringer. The user can specify the element size in both the longitudinal and transverse direction of the specimen. This can be used to apply a higher mesh density at the location at which skin-stringer separation will initiate.

5.2.3 Indenters and contact

Indenters The indenters in the model are representative of the actual loading points and supports in a rigid test frame. These indenters are modeled using analytical rigid surfaces. The position and size of the indenters can easily be changed with the following parameters. The number of supports and the positions are dependent on the type of configuration, if it is 7PB or ECT. Beside the radius of the hemisphere, all these parameters are known from Chapter 4:

- Configuration: 7PB configuration or ECT configuration
- S_X: Longitudinal position of the support
- S_Y: Transverse position of the support
- L_X: Longitudinal position of the point
- L_Y: Transverse position of the loading point
- Radius: Radius of the indenter hemisphere

Contact Based on the position of the skin and stringers, a contact interaction constraint is created between the surface of the elements within a given radius of the indenter. The contact properties consist of a tangential coefficient of friction to prohibit any sliding of the specimen.

- Ind_{sq}: The square around an indenter in which the elements have a contact constraint
- μ_t: Tangential coefficient of friction.

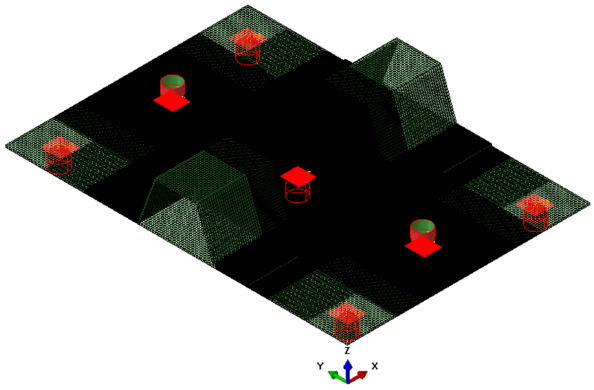

Figure 5.6: 7PB model with contact areas.

5.2.4 Cohesive and tie

This model uses cohesive elements, which allow the modeling of skin-stringer separation. The cohesive elements are initially of zero thickness as they represent an interface. The Python tool creates these zero-thickness 8-noded cohesive elements (COH3D8) by connecting the top nodes of a skin element to the bottom nodes of the stringer element. The user can specify the length of the interface in which these cohesive elements are present. At the part of the interface in which no cohesive elements are present, the skin is rigidly tied to the stringer. The cohesive zone is applied at the skin-stringer interface at both sides of the stringer. For visualization, the cohesive zone at one side is highlighted in Figure 5.7a and the rigid tie constraint in Figure 5.7b. The inner side of the stringer flange contains elements that are typically 5-10 times larger than the adjacent continuum shells. This is done in order to model the corner without a radius or the need of additional through-the-thickness elements. However, if cohesive elements were connected to such a large element, the behavior would be unrealistic. Therefore, the inner corners of the stringer that consists of a single row of elements are rigidly tied to the skin.

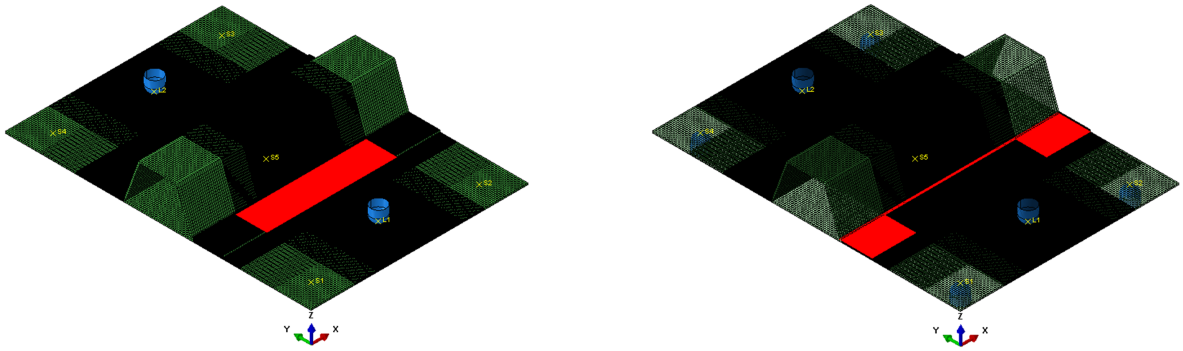

(a) (b)

Figure 5.7: 7PB configuration highlighting the a) cohesive elements and b) rigidly tied region.

5.2.5 Analysis

The analysis block allows the user to define the maximum applied displacement of the indenters as well as the minimum, maximum, initial and total timestep. For this model, a dynamic implicit analysis for a quasi-static load application is used. The dynamic implicit quasi-static analysis is used to obtain improved convergence and stability due to energy dissipation. The time increment is aggressively increased, when only few iterations are needed for an increment [49].

5.3 Seven Point Bending Configuration

This section describes the FE model that is used for the single-stringer specimen in a 7PB configuration to test for mode I skin-stringer separation. The influence of the penalty stiffness of the cohesive elements on the response of the single-stringer specimen is shown. Furthermore, three different loading conditions are used in order to investigate the effect of the positions of the loading points on damage onset and initiation.

5.3.1 Finite element model

The mesh that will be used for the numerical models with different loading conditions of the 7PB configuration are created with the Python input file tool. The dimensions, mesh size and properties are the same as the local model of region 1 as discussed in subsection 5.1.1. However, this numerical model does include the supports and loading points instead of the global/local boundary conditions.

The hemispheres representing the supports and loading points are modeled as analytical rigid surfaces with a diameter of 12.7 mm [9]. The positions of the loading points and supports are defined in Section 4.2, where the optimum variables are equal to $S_Y = 20$ mm and $L_Y = 34$ mm. The surface area of the skin elements that are used for contact is equal to 25.4 mm x 25.4 mm.

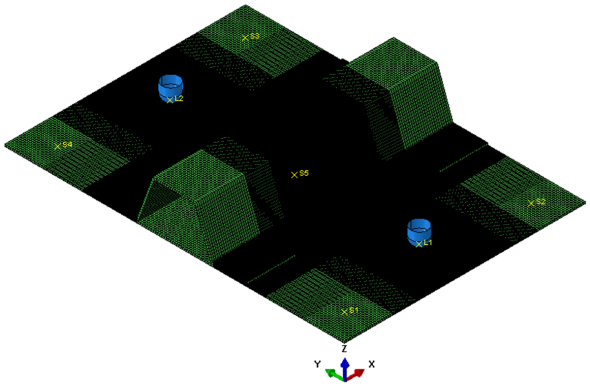

Figure 5.8: FE model of 7PB configuration with continuum shell elements

5.3.2 Cohesive zone length

The response of the single-stringer specimen is dependent on some of the cohesive properties as discussed in Section 2.4. In order to verify that the results are not affected by the penalty stiffness of the cohesive elements, the force-displacement curves of numerical models with and without cohesive elements are compared, shown in Figure fig:7pbnocoh. In the latter, only a rigid tie constraint over the full interface to the model is present. The penalty stiffness of the cohesive elements is high enough to not add artificial compliance to the specimen.

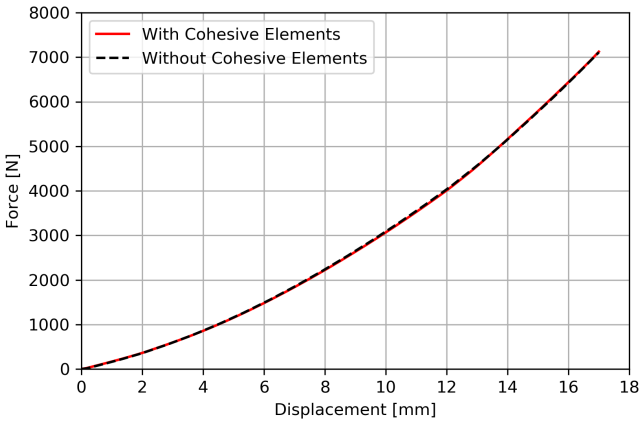

Figure 5.9: Force-displacement response of a single-stringer specimen with and without cohesive elements in a 7PB configuration.

If the penalty stiffness is too high, insufficient elements will be present in the cohesive zone, which will result in an inaccurate model. The cohesive zone length is equal to the distance between the crack tip, where D = 1 and the crack front, where D = 0. The cohesive elements near the location of mode I damage initiation are shown in Figure 5.10, the active cohesive zone is visualized between the gray and black areas, which are the crack tip and crack front respectively. The number of cohesive elements in the cohesive zone is equal to seven, which is more than the minimum required [44].

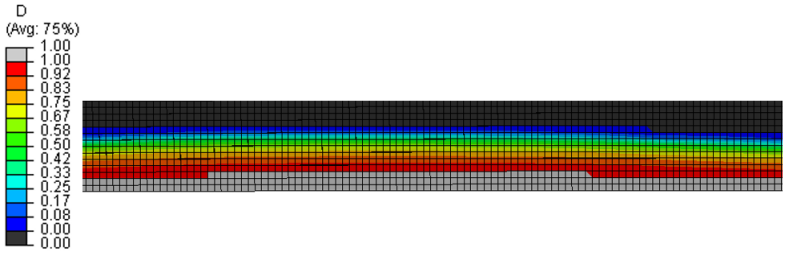

Figure 5.10: Cohesive elements near the location of damage initiation showing the number of active elements between crack front and crack tip.

5.3.3 Loading conditions

In the case of the 7PB configuration, a mode I-dominant type of separation is expected at the longitudinal middle of the specimen. With three different loading conditions for the 7PB configurations, the effect of the loading point position on the location of damage initiation that eventually would lead to skin-stringer separation is investigated:

- Loading Condition 1 (7PB1): $S_Y = 20$ mm and $L_Y = 20$ mm
- Loading Condition 2 (7PB2): $S_Y = 20$ mm and $L_Y = 34$ mm (optimal)
- Loading Condition 3 (7PB3): $S_Y = 20$ mm and $L_Y = 52$ mm

The force-displacement curves for each of the loading conditions are plotted in Figure 5.11. The definitions of damage onset and initiation are described in subsection 5.1.1. The location of damage onset are shown in Figure 5.12. In the case of $L_Y = 20$ mm, damage onset occurs near the edge of the specimen. When the loading point is positioned closer to the stringer flange at $L_Y = 34$ mm, the more critical the mode I opening becomes at the maximum deformation of the imposed buckling wave, but still some damage is seen at the edge. If the loading points are positioned at $L_Y = 52$ mm, the mode I opening at the middle of the specimen occurs before the damage due to shearing at the edge of the cohesive zone.

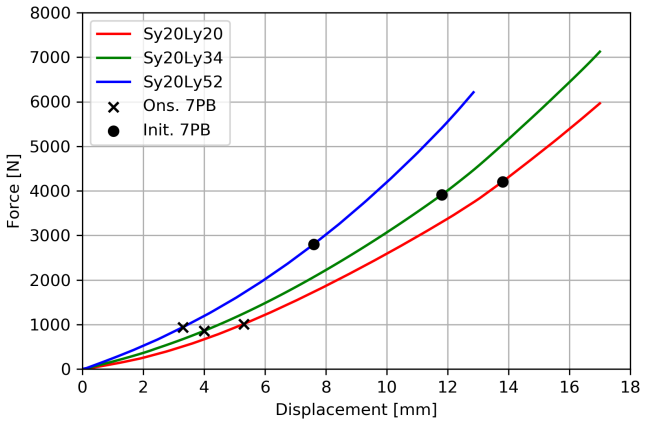

Figure 5.11: Force-displacement response for all three 7PB loading conditions showing damage onset and initiation.

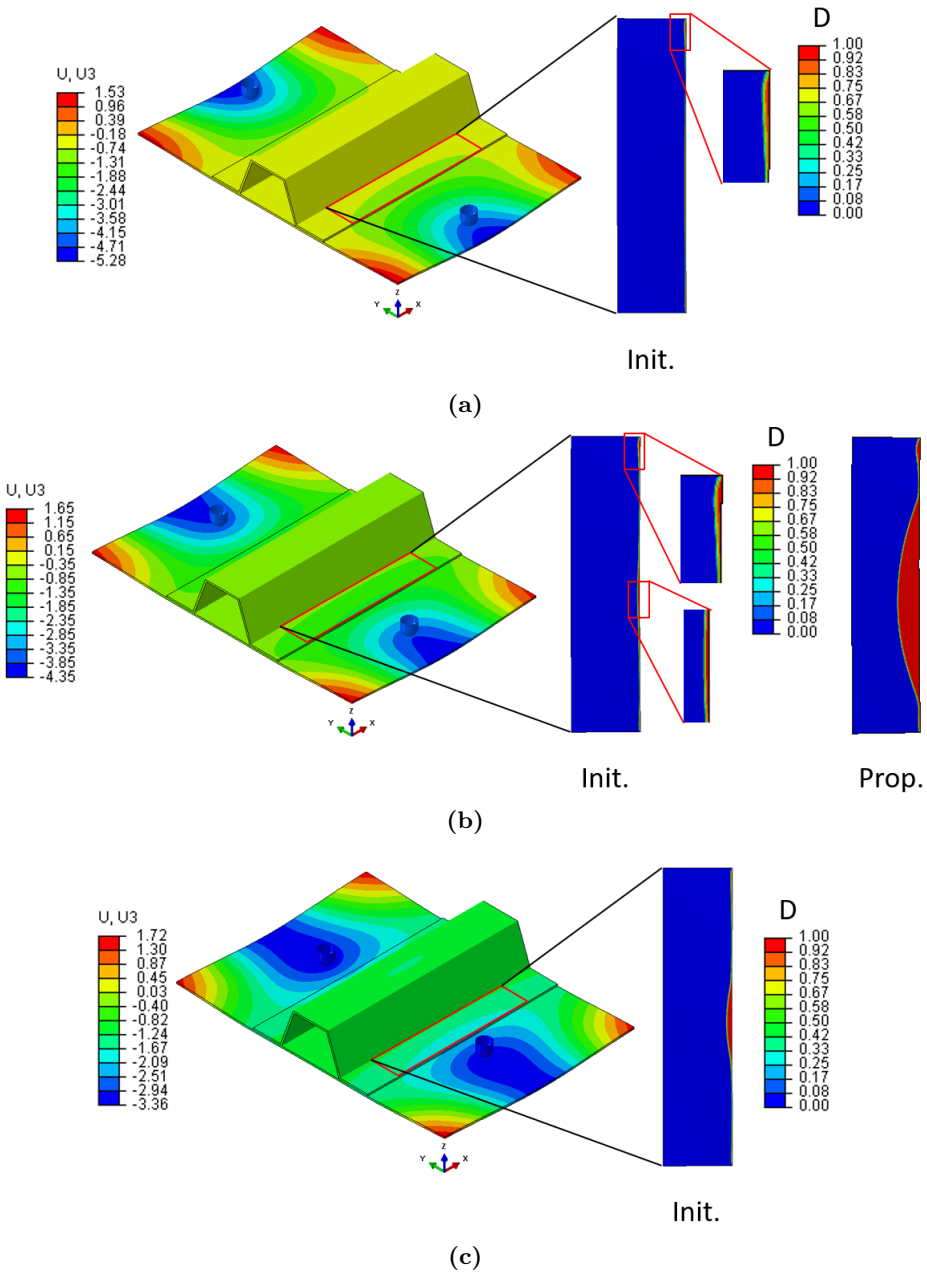

Figure 5.12: Damage initiation for 7PB configuration with a) $S_Y = L_Y = 20$ mm, b) $S_Y = 20$ mm and $L_Y = 34$ mm (optimal) and c) $S_Y = 20$ mm and $L_Y = 52$ mm.

The effect of the transverse position of the loading points on the type of damage initiation is illustrated here. The closer a loading point is near the stringer edge, the more dominant the mode I opening becomes. However, the results of the 7PB configuration cannot be directly compared to the local model of region 1. The 7PB configuration is specifically designed to test the opening mode at the location of maximum deformation. The damage onset in the selected region 1 was primarily at the inflection point and prior to 5 mm end-shortening no mode I opening occurred.

For the optimal configuration, the propagation was also investigated, shown in Figure 5.12c. Even though damage initiation is at the corner of the specimen, damage propagation is mode I driven at the center of the specimen. However, the applied out-of-plane displacement that is needed to obtain this propagation is approximately 21 mm with a corresponding force of 10 kN. The out-of-plane displacement of the loading points that is needed to approximate the deformation field of region 1 at 5 mm end-shortening is equal to 5.5 mm. In order to reduce the applied load and increase the mode I-dominant opening mode, a Teflon insert can be placed at the skin-stringer interface to model initial damage.

5.4 Region 2: Edge Crack Torsion Configuration

This section starts with the description of the FE model, following with the comparison of initiation of skin-stringer separation between the different loading conditions of the ECT configuration. This section is concluded with an overview of the obtained results.

5.4.1 Finite element model

The FE model of the single-stringer specimen in the ECT configuration that is designed to approximate the deformation field of region 2 of the four-stringer panel is similar to the local model of region 2, discussed in subsection 5.1.1. However, the numerical model of the ECT loading conditions include the hemispheres that are used to model the supports and loading points, shown in Figure 5.13.

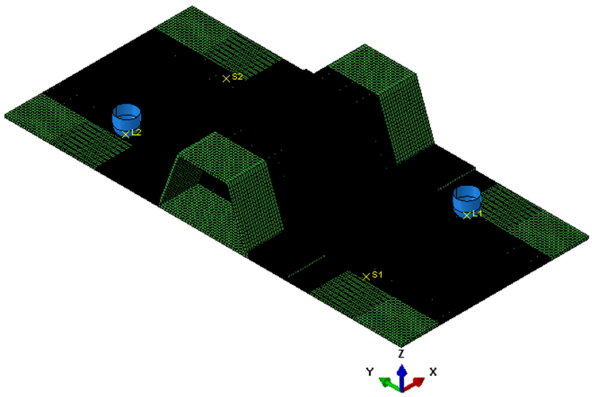

Figure 5.13: FE model of ECT configuration with continuum shell elements.

5.4.2 Loading conditions

For the ECT configuration, three loading conditions are discussed in this subsection, which are taken from the six conditions that were discussed in Chapter 4:

- Loading Condition 1 (ECT1): $S_X = 20$ mm and $S_Y = 20$ mm
- Loading Condition 2 (ECT2): $S_X = 30$ mm and $S_Y = 34$ mm
- Loading Condition 3 (ECT3): $S_X = 30$ mm and $S_Y = 48$ mm (optimal)

The difference in location of damage onset and initiation will be investigated for the different loading conditions. Furthermore, each loading condition will be compared to the local model of region 2.

ECT1

Because the local model and the numerical model of the ECT loading conditions have the same size and mesh, the results can be easily compared. However, the deformation of the local model is driven by the end-shortening of the four-stringer panel, whereas the deformation of the single-stringer specimen in the ECT configuration is driven by out-of-plane displacement. Nevertheless, the nodes in the local model do exhibit out-of-plane deformation that should be similar to the deformation that is observed in the ECT model. Therefore, the out-of-plane displacement of the nodes in the local model can be related to the out-of-plane displacement that is applied by the loading points in the ECT model.

The supports and loading points of ECT1 are placed at $S_X = L_X = 20$ mm and $S_Y = L_Y = 20$ mm. At an applied displacement of these loading points equal to 6.8 mm damage onset occurs. Because the supports are stationary, the applied displacement of the supports is always zero and thus the difference in deformation between the support and loading point is also 6.8 mm. When damage onset occurs in the local model of region 2, corresponding to an end-shortening of 1.2 mm, the node that is located at x = 20 mm, y = 234 mm and z = 0.762 mm in the local model, corresponding to the position of the loading point in ECT1, displaced -1.88 mm. The node that is located at x = 100, y = 234 mm and z = -0.762 mm, corresponding to the support in ECT1, displaced 2.44 mm. The total difference in deformation between these two points in the local model is 4.32 mm at damage onset.

The force-displacement curve of the ECT1 is shown in Figure 5.14. The two vertical lines depict the deformation of the nodes in the local model, with the coordinates of the loading point and support in the ECT1, at damage onset and damage initiation. The relative displacement of these nodes in the local model at damage onset is 4.32 mm. The two points on the curve depict the applied displacement of the loading points and the corresponding force at damage onset and initiation in ECT1. The closer the points that represent damage onset and initiation in the ECT configuration are to the vertical lines that represent onset and initiation in the local model of region 2, the better the approximation would be.

The location at which damage occurs in the local model is shown in Figure 5.4. For the ECT1 model the location of damage initiation is shown in Figure 5.15. Comparing these two figures, it can be observed that damage initiation of the ECT1 model occurs more towards the top (positive x) of the cohesive zone. The out-of-plane deformation of the cohesive zone itself illustrating the inflection point, shown at the far right of Figure 5.15 is close to the location of damage initiation. The next step is to investigate ECT2, which has a lower shape error compared to ECT1, which should result in a better approximation of the damage.

ECT2

The same approach as described for ECT1 is repeated here for this loading condition. The positioned of the loading points and supports are defined by $S_X = 30$ mm and $S_Y = 34$ mm.

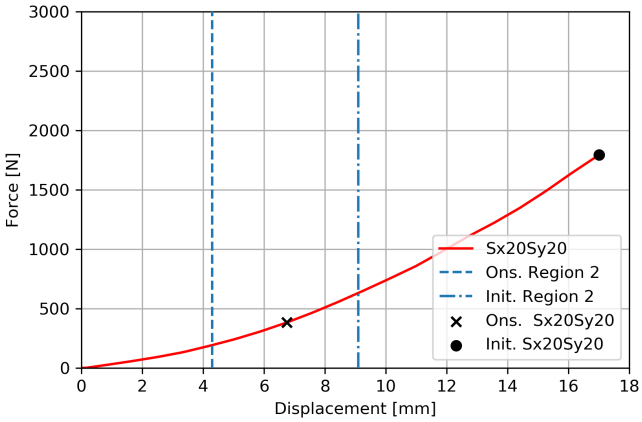

Figure 5.14: Force-displacement response for ECT1 with $S_X = S_Y = 20$ mm showing damage onset and initiation for the ECT1 model and the local model of region 2.

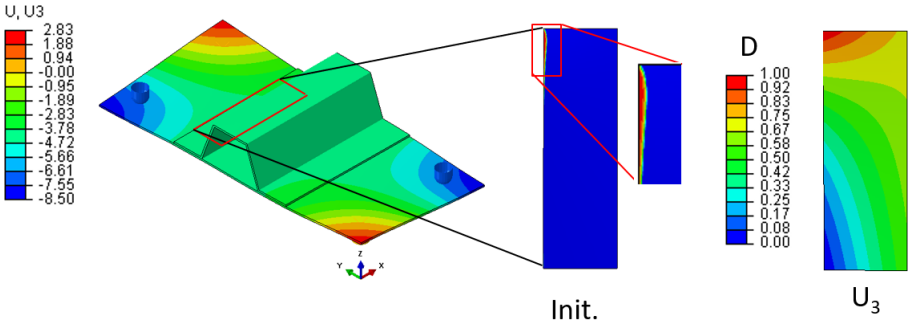

Figure 5.15: Damage initiation for ECT1 with $S_X = S_Y = 20$ mm.

At damage onset of the local model, the node located at x = 30 mm, y = 220 mm and z = 0.762 mm in the local model of region 2, corresponding to the coordinates of the loading point in ECT2, displaced -1.46 mm. The node that is located at x = 90, y = 220 mm and z = -0.762 mm, corresponding to the coordinates of the support in ECT2, displaced 1.88 mm. The difference in deformation of these two nodes of the local model at damage onset is 3.34 mm. The force-displacement curve of the ECT2 model is shown in Figure 5.16 including the damage onset and initiation of the ECT2 model and the local model of region 2. The difference in deformation at damage onset between the ECT2 model and the local model is smaller compared to the difference between the ECT1 model and the local model.

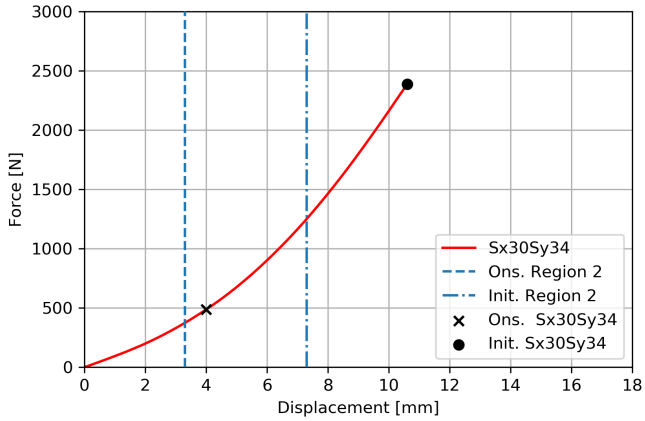

Figure 5.16: Force-displacement curve for ECT2 with $S_X = 30$ mm and $S_Y = 34$ mm showing damage onset and initiation for the ECT2 model and the local model of region 2.

The location of damage onset in the ECT2 model is shown in Figure 5.17. Maximum inflection in the cohesive zone is located more towards the center of the model compared to Figure 5.15. This resulted in a slight shift of damage onset location also towards the center. This is already more similar to the local model of region 2, compared to the approximation of the ECT1 model. The next step is to investigate if the loading condition that was found in Chapter 4 to be optimal in approximating the deformation field of region 2 is also the most optimal in approximating the damage initiation.

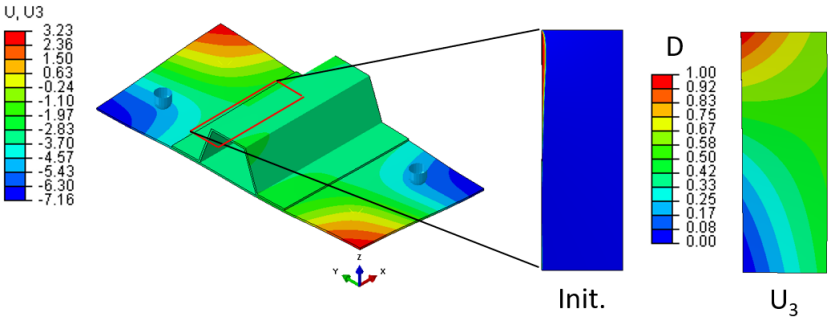

Figure 5.17: Damage initiation for ECT2 with $S_X = 30$ mm and $S_Y = 34$ mm.

ECT3

Initiation The force-displacement curve of the optimal loading condition is shown in Figure 5.18. The locations of the nodes in the local model that correspond to the coordinates of the loading point and the support in the ECT3 model respectively are: x = 30 mm, y = 204 mm and z = 0.762 mm and x = 90 mm, y = 204 mm and z = -0.762 mm. The displacement of the loading points at damage onset and initiation in ECT3 are illustrated with the points on the curve in Figure 5.18. The vertical lines in Figure 5.18 correspond to out-of-plane displacement of the two nodes in the local model of region 2. The difference in deformation of the nodes between the local model and the ECT3 model at damage onset and initiation is smaller compared to the differences that are observed in the ECT1 and ECT2 model. The location of damage initiation in the ECT3 model, shown in Figure 5.19, also displays the most resemblance with the local model of region 2.

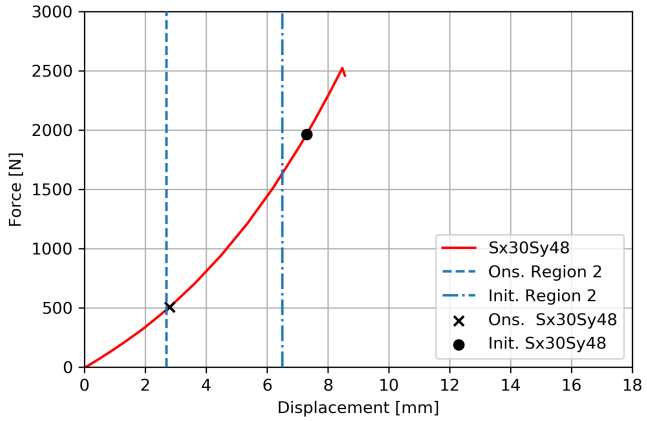

Figure 5.18: Force-displacement curve for ECT3 with $S_X = 30$ mm and $S_Y = 48$ mm showing damage onset and initiation for the ECT3 model and the local model of region 2.

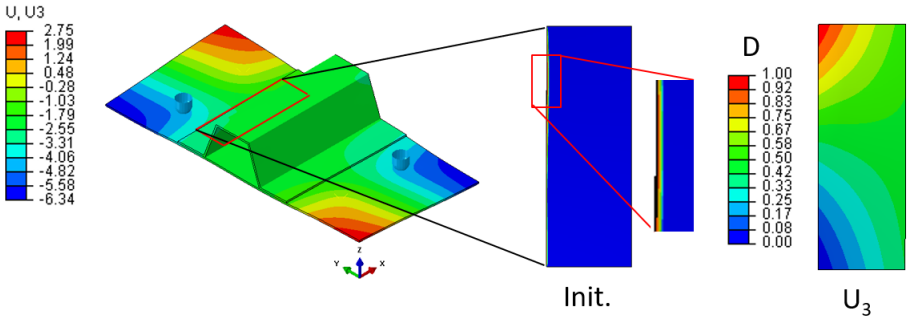

Figure 5.19: Damage initiation for the optimal ECT3 with $S_X = 30$ mm and $S_Y = 48$ mm.

Propagation The crack propagation for the cohesive interface for the optimal loading condition is shown in Figure 5.20. After crack initiation at 7.3 mm, rapid crack growth starts from 8.54 mm onwards. The crack growth at either side of the stringer is antisymmetric

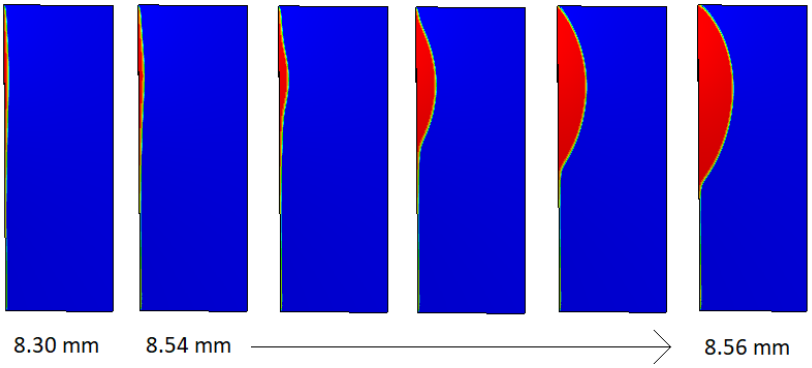

Figure 5.20: Cohesive interface showing the crack propagation for ECT3 with $S_X = 30$ mm and $S_Y = 48$.

with respect to the x-axis. The crack propagation is limited at the edge of the cohesive zone, because the skin is rigidly tied to the stringer near the free edge of the single-stringer specimen. Because the location of initiation and the subsequent propagation does not occur at the center of the specimen, the width of the specimen has to be reconsidered in order to minimize the edge effects during damage growth. Due to aforementioned reasons in Section 5.1, the propagation of the specimen in the ECT configuration can not be compared to the local model of the four-stringer panel.

Overview

The difference in percentage between all the deformation of the ECT models and the local modal is calculated by:

$$\frac{U_{3_{local}} - U_{3_{ECT}}}{U_{3_{local}}} \times 100\% = \varepsilon \tag{5.1}$$

where $U_{3_{local}}$ is the total displacement of the two nodes in the local model at damage onset and damage initiation in the local model. $U_{3_{ECT}}$ is the displacement of the loading points in the ECT configuration at damage onset and damage initiation. The results are presented in Table 5.2.

Table 5.2: Overview of deformation error between local model of region 2 and the ECT models at damage onset and damage initiation.

	Damage onset			Damage initiation		
Loading Condition	$U_{3_{local}}$	$U_{3_{ECT}}$	ε	$U_{3_{local}}$	$U_{3_{ECT}}$	ε
ECT1	4.3 mm	6.8 mm	-57%	9.1 mm	17.0 mm	-87%
ECT2	3.3 mm	4.0 mm	-21%	7.3 mm	10.6 mm	-45%
ECT3	2.7 mm	2.8 mm	-4%	6.5 mm	7.3 mm	-12%

The ECT loading condition that lead to the best approximation of the deformation field of region 2, discussed in Chapter 4, also shows the best approximation in damage onset

and initiation of region 2. Care must be taken, because only three different configurations were investigated here. However, the methodology that is created here that is based on approximating the buckling deformation to investigate the damage initiation is promising.

5.5 Concluding Remarks

This section presents the conclusion of this chapter, including a discussion and further improvements for the cohesive zone model.

5.5.1 Conclusion

This chapter describes the second step in the methodology that is under development to study skin-stringer separation in postbuckled composite stiffened structures using single-stringer specimens. The goal of this effort was to develop single-stringer specimens that are less expensive to manufacture and test than the corresponding multi-stringer panel. Because these specimens are intended to be tested under out-of-plane displacement control and for specific loading conditions, they can potentially provide a more precise substantiation of damage tolerance of individual modes of failure in a multi-stringer panel. Finally, these specimens require models that are computationally less demanding than larger structures, which allows the use of fine meshes required to investigate the performance of detailed damage models that can predict skin-stringer separation. For both the 7PB and the ECT configuration three distinct loading conditions were examined in which initiation of skin-stringer separation was modeled using cohesive elements at the interface.

For the 7PB configurations, it was found that placing the loading point closer to the stringer flange leads to a more dominant mode I type of damage. However in the performed global/local analysis of region 1 of the four-stringer panel the expected mode I opening was not present. This can be a result of having no mismatch in flexural stiffness between the skin and stringer flange. Nonetheless, there are more locations in the four-stringer panel at which the buckling wave deformation is maximum and thus potentially a mode I opening can occur. These other locations have to be investigated in order to find the most critical damage mode for this panel. Furthermore, a study on the effect of initial cracks in the form of Teflon inserts has to be conducted. These initial cracks can promote a mode I opening if they are close to a location of maximum deformation.

For the ECT configuration, the loading condition that was found to be optimal in approximating deformation at the inflection point of the four-stringer panel also showed the most similarity in location of damage initiation compared to the region 2 local model of the four-stringer panel. Moreover, the difference in deformation between the loading points of the optimal ECT loading condition and the corresponding nodes of the local model at damage onset and initiation was also smallest. The conclusion can be drawn that developing a configuration based on approximating the buckling deformation to test skin-stringer separation is a promising method.

5.5.2 Discussion

More work has to be done in the design of this methodology to study of skin-stringer separation. The next step is to investigate the effect of initial cracks using a Teflon insert on the type of separation. Furthermore, experimental tests need to be conducted in order to validate the response of the 7PB and ECT configurations.

Other approaches to this method can also be used, such as approximating the actual onset of skin-stringer separation behavior instead of only the buckling deformation field to find the optimal position of the supports and loading points, which was described in Chapter 4. The former approach would be more accurate as the goal is to actual characterize the skin-stringer separation and not the buckling deformation. However, conducting an optimization study while using cohesive elements to allow skin-stringer separation can also be computationally demanding.

The investigation into skin-stringer separation in the four-stringer panel can also be improved. Currently, only damage initiation is studied in the specified regions using the global/local method. Another method would be to simulate the full four-stringer panel and position cohesive elements at the skin-stringer interface. Using this method, the stiffness matrix of the four-stringer panel FE model is constantly updated during the propagation of damage. This would be more computationally demanding, but would also shine more light onto the damage propagation that occurs in the multi-stringer panel.

5.5.3 Further improvements of the cohesive zone model

The current approach was only to show that skin-stringer separation in the region of maximum deformation and the region of maximum twisting of the skin found in a four-stringer panel can be estimated numerically with the use of single-stringer specimen. However, the currently used cohesive zone model can be improved in order to provide a more accurate approximation of the actual skin-stringer separation that would occur during an experimental test.

Firstly, the Benzeggagh-Kenane criterion that is used for calculating the damage propagation under mixed-mode loading assumes that the critical energy release rate for the two shear modes are equal. Literature study has shown that this is not necessarily the case as the value of critical energy release rate for mode III can be up to 1.5 times the value of mode II [33,57]. Albeit, there already have been some efforts in modifying the Benzeggagh-Kenane formula to include a separate value for mode III critical energy release rate [58]. This subject must be explored more if the research on mode III-dominant skin-stringer separation is continued.

Secondly, the cohesive properties that are determined using End-Notched Flexure, Double Cantilever Beam and Mixed-Mode Bending tests often use the traditional crack interface of $0°/0°$ to estimate the critical energy release rate of material. For nontraditional interfaces, such as used in this research, these properties can increase by fourfold [9].

Lastly, the current bilinear cohesive law only takes into account simple opening, whereas the actual crack propagation is far more complex because it involves fiber bridging, matrix cracking, blunting of the crack and delving. This type of behavior can be modeled using

more complex cohesive laws that take into account the R-curve. A procedure that is used for this type of research is superposing two sets of bilinear cohesive laws resulting in a trilinear law [9]. This is done by using two sets of cohesive elements at the interface.

There is still a long trajectory to walk before it is possible to grasp the complex behavior of skin-stringer separation, especially with the limited knowledge on mode III-dominant failure modes. The current work that is ongoing in improving the cohesive laws and damage modeling techniques are certainly contributing.

Chapter 6

Conclusions

The goal of this thesis is to develop a numerical method to investigate possible skin-stringer separation in multi-stringer panels. The first step was to study the postbuckling deformation of a four-stringer panel loaded in compression. Two distinct regions were identified in the panel: maximum displacement of the skin away from the stringer and maximum twisting of the skin at the inflection point of a buckling wave. When the skin bends away from the stringer, the interface can open, eventually leading to separation of the stringer, which is mode I-dominated. At the location of maximum twisting, interlaminar shear stresses are present that can also lead to separation in a mode II + III type of loading. However, this type of skin-stringer separation has received little attention.

These two regions were approximated using a model of a single-stringer specimen in a loading configuration. With this configuration an out-of-plane deformation can be applied to the specimen that results in a deformed shape similar to the deformation in the aforementioned regions. The shape of the buckling deformation will affect the location of crack initiation. The first region, where the out-of-plane deformation of the skin is at its maximum was approximated with the use of a single-stringer specimen in a seven-point bending configuration. In this configuration, five supports and two loadings points impose an out-of-plane deformation. The second region, characterized by twisting of the skin, was approximated using an edge crack torsion configuration, in which two supports and two loading points apply out-of-plane displacements. The optimal position of the supports and loading points for these configurations was determined by minimizing the difference between the out-of-plane displacement of the single-stringer configurations and the out-of-plane displacement in corresponding regions in the four-stringer panel.

Crack initiation that can lead to skin-stringer separation was modeled for both the seven-point bending and the edge crack torsion configurations. This finite element model includes cohesive elements that use the bilinear traction-separation law to track the interlaminar damage response. The optimal loading conditions of each configuration were compared to two other sub-optimal conditions to see the effect of the position of the supports and loading points on the location of crack initiation. Next to this, a global/local analysis was performed, which

uses the response of the four-stringer panel as the boundary conditions for the complex single-stringer specimens. This decouples the buckling deformation observed in the global model of the four-stringer panel from the damage initiation in a local model that uses cohesive elements. The two local models are the regions of maximum displacement and of maximum twisting of the skin.

The local model of the region of maximum displacement did not show any mode I-dominant opening of the skin-stringer interface prior to an end-shortening of 5 mm of the four-stringer panel. However, only one location of maximum buckling wave deformation has been investigated. Other locations could still be mode I critical, especially if an initial defect is present, which can be modeled using a Teflon insert at the skin-stringer interface. The local model of the region of maximum twisting did show a shear-dominant mode at the inflection point of a buckling wave at an end-shortening of 3.5 mm.

The effect of the position of the loading points in the 7PB configuration on the location of crack initiation was investigated. It was observed that a smaller distance between the stringer flange and the loading point promotes the mode I opening of the interface. For the ECT configuration, the effect of the position of the supports and the loading points on crack initiation was also investigated. Three distinct loading conditions were compared, in which one was found to be the most optimal in approximating the buckling deformation of the region of maximum twisting in the four-stringer panel. The most optimal loading condition also showed the best similarity in deformation compared to the local model of the region of maximum twisting at damage initiation. Furthermore, the location of crack initiation was also most similar for the most optimal loading condition. Therefore, the proposed methodology to determine a loading conditions by minimizing the difference in the out-of-plane deformation between a single-stringer specimen and a multi-stringer panel is promising.

References

[1] A.K. Noor, J.H. Starnes, and J.M. Peters. Uncertainty analysis of stiffened composite panels. *Composite Structures*, 51(2):139–158, 2001.

[2] S. Wanthal, J. Schaefer, B. Justusson, I. Hyder, S. Engelstad, and C. Rose. Verification and validation process for progressive damage and failure analysis methods in the NASA Advanced Composites Consortium. In *32nd American Society for Composites Conference, West Lafayette, IN*, 2017.

[3] R. Krueger and P.J. Minguet. Analysis of composite skin–stiffener debond specimens using a shell/3D modeling technique. *Composite Structures*, 81(1):41–59, 2007.

[4] C. Bisagni and R. Vescovini. Analytical formulation for local buckling and post-buckling analysis of stiffened laminated panels. *Thin-Walled Structures*, 47(3):318–334, 2009.

[5] Military. CHM-17-3F: Composite materials handbook, polymer matrix composites: Materials usage, design, and analysis. *US Department of Defense*, 2002.

[6] J. Bertolini, B. Castanié, J.J. Barrau, and J.P. Navarro. Multi-level experimental and numerical analysis of composite stiffener debonding. Part 1: Non-specific specimen level. *Composite Structures*, 90(4):381–391, 2009.

[7] P.J. Minguet and T.K. O'Brien. Analysis of test methods for characterizing skin/stringer debonding failures in reinforced composite panels. In *Composite Materials: Testing and Design: Twelfth Volume*. ASTM International, 1996.

[8] J. Bertolini, B. Castanié, J.J. Barrau, and J.P. Navarro. An experimental and numerical study on omega stringer debonding. *Composite Structures*, 86(1):233–242, 2008.

[9] C.G. Dávila, F.A. Leone, K. Song, J.G. Ratcliffe, and C.A. Rose. Material characterization for the analysis of skin/stiffener separation. In *in 32nd American Society for Composites Conference, West Lafayette, IN.*, 2017.

[10] J.C.F.N. van Rijn and J.F.M. Wiggenraad. A seven-point bending test to determine the strength of the skin-stiffener interface in composite aircraft panels. *Technical Publication 2000-044*, 2000.

[11] J. Bertolini, B. Castanié, J.J. Barrau, J.P. Navarro, and C. Petiot. Multi-level experimental and numerical analysis of composite stiffener debonding. part 2: Element and panel level. *Composite Structures*, 90(4):392–403, 2009.

[12] Q. Ye and P. Chen. Prediction of the cohesive strength for numerically simulating composite delamination via CZM-based FEM. *Composites Part B: Engineering*, 42(5):1076–1083, 2011.

[13] C. Bisagni. Progressive delamination analysis of stiffened composite panels in postbuckling. In *Proceedings of the AIAA/ASME/ASCE/AHS/ASC 47th Structures, Structural Dynamics and Materials Conference, AIAA paper*, number 2006-2178, 2006.

[14] C. Bisagni, R. Vescovini, and C.G. Dávila. Single-stringer compression specimen for the assessment of damage tolerance of postbuckled structures. *Journal of Aircraft*, 48(2):495–502, 2011.

[15] A. Velicki. Damage arresting composites for shaped vehicles. *Technical Publication NASA/CR-2009-215932*, 2009.

[16] D. C Jegley. Experimental behavior of fatigued single stiffener prseus specimens. *Technical Publication NASA/TM-2009-215955*, 2009.

[17] A. Velicki and D. Jegley. PRSEUS structural concept development. In *52nd AIAA Aerospace Sciences Meeting (National Harbor, MD)*, 2014.

[18] B. Qi, R. Ness, and L. Tong. A stitched blade-stiffened RFI composite panel under shear loading. *Journal of Reinforced Plastics and Composites*, 21(3):255–276, 2002.

[19] C. Bisagni, R. Vescovini, and C. Dávila. Assessment of the damage tolerance of postbuckled hat-stiffened panels using single stringer specimens. In *AIAA-2010-2696, 51st AIAA/ASME/ASCE/AHS/ASC Structures, Structural Dynamics, and Materials Conference 18th AIAA/ASME/AHS Adaptive Structures Conference, 12-15 April , Orlando, Florida*, 2010.

[20] R. Vescovini, C.G. Dávila, and C. Bisagni. Failure analysis of composite multi-stringer panels using simplified models. *Composites Part B: Engineering*, 45(1):939–951, 2013.

[21] C. Bisagni and C.G. Dávila. Experimental investigation of the postbuckling response and collapse of a single-stringer specimen. *Composite Structures*, 108:493–503, 2014.

[22] C.G. Dávila and C. Bisagni. Fatigue life and damage tolerance of postbuckled composite stiffened structures with indentation damage. *Journal of Composite Materials*, 52(7):931âĂŞ–943, 2018.

[23] S.L. Donaldson. Mode III interlaminar fracture characterization of composite materials. *Composites Science and Technology*, 32(3):225–249, 1988.

[24] P. Robinson and D.Q. Song. The development of an improved mode III delamination test for composites. *Composites Science and Technology*, 52(2):217–233, 1994.

[25] A. Szekrényes. Improved analysis of the modified split-cantilever beam for mode-III fracture. *International Journal of Mechanical Sciences*, 51(9):682–693, 2009.

[26] G. Becht and J.W. Gillespie. Design and analysis of the crack rail shear specimen for mode III interlaminar fracture. *Composites Science and Technology*, 31(2):143–157, 1988.

[27] D. Zhao and Y. Wang. Mode III fracture behavior of laminated composite with edge crack in torsion. *Theoretical and Applied Fracture Mechanics*, 29(2):109–123, 1998.

[28] M.W. Czabaj, J.G. Ratcliffe, and B.D. Davidson. Observation of intralaminar cracking in the edge crack torsion specimen. *Engineering Fracture Mechanics*, 120:1–14, 2014.

[29] M.W. Czabaj, B.D. Davidson, and J.G. Ratcliffe. A modified edge crack torsion test for measurement of mode-III fracture toughness of laminated tape composites. In *31st Annual Technical Conference of the American Society for Composites, ASC 2016*. DEStech Publications Inc., 2016.

[30] J. Li, S.M. Lee, E.W. Lee, and T.K. O'Brien. Evaluation of the edge crack torsion (ECT) test for mode III interlaminar fracture toughness of laminated composites. *Journal of Composites, Technology and Research*, 19(3):174–183, 1997.

[31] J.G. Ratcliffe. Characterization of the edge crack torsion (ECT) test for mode III fracture toughness measurement of laminated composites. *NASA/Technical Memorandum*, 213269, 2004.

[32] G. Browning, L.A. Carlsson, and J.G. Ratcliffe. Modification of the edge crack torsion specimen for mode III delamination testing. Part II–experimental study. *Journal of Composite Materials*, 45(25):2633–2640, 2011.

[33] A.B. De Morais, A.B. Pereira, M.F.S.F. De Moura, and A.G. Magalhães. Mode III interlaminar fracture of carbon/epoxy laminates using the edge crack torsion (ECT) test. *Composites Science and Technology*, 69(5):670–676, 2009.

[34] A.B. Pereira, A.B. de Morais, and M.F.S.F. de Moura. Design and analysis of a new six-point edge crack torsion (6ECT) specimen for mode III interlaminar fracture characterisation. *Composites Part A: Applied Science and Manufacturing*, 42(2):131–139, 2011.

[35] A.B. De Morais and A.B. Pereira. Mixed mode II+ III interlaminar fracture of carbon/epoxy laminates. *Composites Science and Technology*, 68(9):2022–2027, 2008.

[36] ASTM Standard. D7905/d7905m–14. *Standard Test Method for Determination of the Mode II Interlaminar Fracture Toughness of Unidirectional Fiber-Reinforced Polymer Matrix Composites ASTM International, West Conshohocken*, 2014.

[37] D.R. Ambur, N. Jaunky, and M.W. Hilburger. Progressive failure studies of stiffened panels subjected to shear loading. *Composite Structures*, 65(2):129–142, 2004.

[38] A. de Paula Guedes Villani, M.V. Donadon, M.A. Arbelo, P. Rizzi, C.V. Montestruque, F. Bussamra, and M.R.B. Rodrigues. The postbuckling behaviour of adhesively bonded stiffened panels subjected to in-plane shear loading. *Aerospace Science and Technology*, 46:30–41, 2015.

[39] R. Krueger. Virtual crack closure technique: history, approach, and applications. *Applied Mechanics Reviews*, 57(2):109–143, 2004.

[40] W. Brocks. The cohesive model. In *Solid Mechanics and its Applications*, volume 244, serial 9, pages 151–170. 2018.

[41] A. Turon, P.P. Camanho, J. Costa, and C.G. Dávila. A damage model for the simulation of delamination in advanced composites under variable-mode loading. *Mechanics of Materials*, 38(11):1072–1089, 2006.

[42] M.L. Benzeggagh and M. Kenane. Measurement of mixed-mode delamination fracture toughness of unidirectional glass/epoxy composites with mixed-mode bending apparatus. *Composites Science and Technology*, 56(4):439–449, 1996.

[43] A. Riccio, A. Raimondo, G. Di Felice, and F. Scaramuzzino. A numerical procedure for the simulation of skin–stringer debonding growth in stiffened composite panels. *Aerospace Science and Technology*, 39:307–314, 2014.

[44] A. Turon, C.G. Davila, P.P. Camanho, and J. Costa. An engineering solution for mesh size effects in the simulation of delamination using cohesive zone models. *Engineering Fracture Mechanics*, 74(10):1665–1682, 2007.

[45] M.L. Falk, A. Needleman, and J.R. Rice. A critical evaluation of cohesive zone models of dynamic fracture. *Le Journal de Physique IV*, 11(5):43–50, 2001.

[46] G. Alfano and M.A. Crisfield. Finite element interface models for the delamination analysis of laminated composites: mechanical and computational issues. *International Journal for Numerical Methods in Engineering*, 50(7):1701–1736, 2001.

[47] Z. Zou, S.R. Reid, S. Li, and P.D. Soden. Modelling interlaminar and intralaminar damage in filament-wound pipes under quasi-static indentation. *Journal of Composite Materials*, 36(4):477–499, 2002.

[48] P.P. Camanho, C.G. Davila, and M.F. De Moura. Numerical simulation of mixed-mode progressive delamination in composite materials. *Journal of Composite Materials*, 37(16):1415–1438, 2003.

[49] *ABAQUS/Standard User's Manual, Version 2017*. Simulia, 2017.

[50] H.A. Israr, K.J. Wong, and M.N. Tamin. Cohesive zone modelling of mode III delamination using the edge crack torsion test. *Journal of Mechanical Engineering and Sciences*, 11(1):2526–2538, 2017.

[51] A.C. Orifici, R.S. Thomson, I. Herszberg, T. Weller, R. Degenhardt, and J. Bayandor. An analysis methodology for failure in postbuckling skin–stiffener interfaces. *Composite Structures*, 86(1):186–193, 2008.

[52] C.G. Dávila and C. Bisagni. Fatigue life and damage tolerance of postbuckled composite stiffened structures with initial delamination. *Composite Structures*, 161:73–84, 2017.

[53] S.B. Clay and P.M. Knoth. Experimental results of quasi-static testing for calibration and validation of composite progressive damage analysis methods. *Journal of Composite Materials*, 51(10):1333–1353, 2017.

[54] C. Meeks, E. Greenhalgh, and B.G. Falzon. Stiffener debonding mechanisms in post-buckled CFRP aerospace panels. *Composites Part A: Applied Science and Manufacturing*, 36(7):934–946, 2005.

[55] N.R. Draper and H. Smith. *Applied Regression Analysis*, volume 326. John Wiley & Sons, 2014.

[56] S. Hühne, J. Reinoso, E. Jansen, and R. Rolfes. A two-way loose coupling procedure for investigating the buckling and damage behaviour of stiffened composite panels. *Composite Structures*, 136:513–525, 2016.

[57] T.E. Tay. Characterization and analysis of delamination fracture in composites: an overview of developments from 1990 to 2001. *Applied Mechanics Reviews*, 56(1):1–32, 2003.

[58] Q.V. Bui. A modified Benzeggagh-Kenane fracture criterion for mixed-mode delamination. *Journal of Composite Materials*, 45(4):389–413, 2011.